Cell

Article

Cryo-EM structures reveal multiple stages of bacterial outer membrane protein folding

Graphical abstract

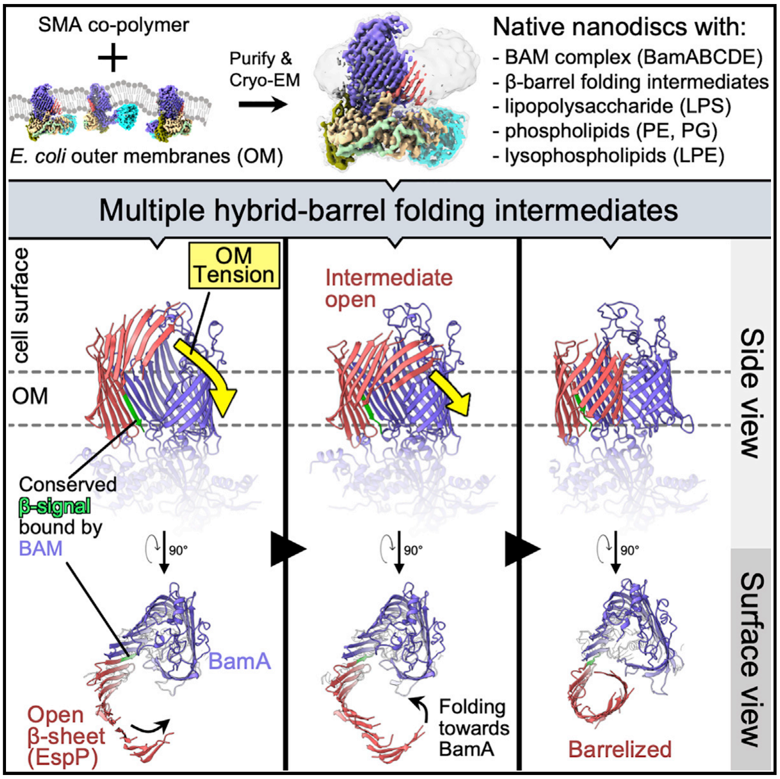

Authors

Matthew Thomas Doyle, John R. Jimah, Tyrone Dowdy, Shannon I. Ohlemacher, Mioara Larion, Jenny E. Hinshaw, Harris D. Bernstein

Correspondence

jenny.hinshaw@nih.gov (J.E.H.),
harris_bernstein@nih.gov (H.D.B.)

In brief

The folding of the β barrel protein EspP by the β barrel assembly machinery in *E. coli* involves the progressive conversion of a β sheet into a barrel-like structure in a process that is influenced by membrane tension.

Highlights

- BAM binds to β signals to orient outer membrane protein β barrels in the membrane
- β barrels fold by passing through an extended β sheet stage while bound to BamA
- Extreme membrane remodeling is a key feature of transmembrane β barrel assembly
- Outer membrane tension accelerates the final stages of bacterial β barrel folding

Doyle et al., 2022, Cell *185*, 1143–1156
March 31, 2022 © 2022 Published by Elsevier Inc.
https://doi.org/10.1016/j.cell.2022.02.016

CellPress

Cell

CellPress

Article

Cryo-EM structures reveal multiple stages of bacterial outer membrane protein folding

Matthew Thomas Doyle,[1,5] John R. Jimah,[2,5] Tyrone Dowdy,[3] Shannon I. Ohlemacher,[4] Mioara Larion,[3] Jenny E. Hinshaw,[2,*] and Harris D. Bernstein[1,6,*]

[1]Genetics and Biochemistry Branch, National Institute of Diabetes and Digestive and Kidney Diseases, National Institutes of Health, Bethesda, MD 20892, USA

[2]Laboratory of Cell and Molecular Biology, National Institute of Diabetes and Digestive and Kidney Diseases, National Institutes of Health, Bethesda, MD 20892, USA

[3]Neuro-Oncology Branch, National Cancer Institute, National Institutes of Health, Bethesda, MD 20892, USA

[4]Laboratory of Bioorganic Chemistry, National Institute of Diabetes and Digestive and Kidney Diseases, National Institutes of Health, Bethesda, MD 20892, USA

[5]These authors contributed equally

[6]Lead contact

*Correspondence: jenny.hinshaw@nih.gov (J.E.H.), harris_bernstein@nih.gov (H.D.B.)

https://doi.org/10.1016/j.cell.2022.02.016

SUMMARY

Transmembrane β barrel proteins are folded into the outer membrane (OM) of Gram-negative bacteria by the β barrel assembly machinery (BAM) via a poorly understood process that occurs without known external energy sources. Here, we used single-particle cryo-EM to visualize the folding dynamics of a model β barrel protein (EspP) by BAM. We found that BAM binds the highly conserved "β signal" motif of EspP to correctly orient β strands in the OM during folding. We also found that the folding of EspP proceeds via "hybrid-barrel" intermediates in which membrane integrated β sheets are attached to the essential BAM subunit, BamA. The structures show an unprecedented deflection of the membrane surrounding the EspP intermediates and suggest that β sheets progressively fold toward BamA to form a β barrel. Along with *in vivo* experiments that tracked β barrel folding while the OM tension was modified, our results support a model in which BAM harnesses OM elasticity to accelerate β barrel folding.

INTRODUCTION

The insertion and folding of integral membrane proteins require precise management of hydrophobic and hydrophilic interfaces during intermediate steps to arrive at a topologically correct and functional structure. The biogenesis of proteins located in the outer membrane (OM) of Gram-negative bacteria and organelles of bacterial origin is especially enigmatic, in part because they rapidly insert into the OM in the absence of known external energy sources (Horne et al., 2020; Tomasek and Kahne, 2021). For unknown reasons, almost all bacterial outer membrane proteins (OMPs) span the membrane via a distinctive "β barrel" structure. Although they can vary greatly in size (8–36 β strands) and can be linked to soluble domains, transmembrane β barrels generally conform to common architectural rules (Horne et al., 2020; Lauber et al., 2018; Schulz, 2000). OMP β barrels are tilted amphipathic antiparallel β sheets that are closed by tight hydrogen bonding between the first and last β strands (the "β seam") into super-stable cylinders that are stabilized in the OM by parallel "girdles" of membrane-facing aromatic residues (Schulz, 2000). Most β barrels also have a highly conserved C-terminal motif called the "β signal" that contains an essential terminal aromatic residue (frequently a phenylalanine) of unknown function (Struyvé et al., 1991; Paramasivam et al., 2012). In bacteria, the assembly (folding and integration) of β barrels is catalyzed by a heterooligomer called the β barrel assembly machinery (BAM) (Voulhoux et al., 2003; Wu et al., 2005). In *E. coli*, BAM is composed of an essential subunit (BamA) and four lipoproteins (BamBCDE) (Wu et al., 2005). BamA is conserved in all Gram-negative bacteria, and essential homologs are also found in mitochondria and chloroplasts (Heinz and Lithgow, 2014; Kozjak et al., 2003; Patel et al., 2008). BamD is likewise highly conserved throughout bacteria but is conditionally essential in *E. coli* (Anwari et al., 2012; Hart et al., 2020; Hart and Silhavy, 2020). BamA is itself an OMP that contains a C-terminal β barrel and generally five soluble N-terminal polypeptide transport-associated (POTRA) domains that bind the lipoproteins (Kim et al., 2007; Webb et al., 2012).

The structural dynamics that occur as OMPs transition from an incompletely folded state to a fully folded β barrel remain unclear. However, available evidence suggests that OMP β signals may be recognized by BAM and that the unusual conformational malleability of BAM (particularly BamA) may facilitate the folding process (Doerner and Sousa, 2017; Doyle and Bernstein, 2019;

Hagan et al., 2015; Iadanza et al., 2016; Kaur et al., 2021; Tomasek et al., 2020; White et al., 2021). Interestingly, BamA does not contain a canonical β signal at its C terminus, but instead has a "kinked" structure that causes its terminal residues to move dynamically and generate an unstable β seam with weak hydrogen bonding (Lundquist et al., 2018; Noinaj et al., 2013). BamA can also adopt either inward-open or outward-open conformational states (in which the BamA β barrel lumen is open to the inside of the cell but closed on the surface or vice versa) that coincide with the opening and closing of its β seam (Gu et al., 2016). Experiments in which the BamA β seam was tethered closed by disulfide bonds indicate that the opening and closing of BamA is required for efficient β barrel folding (Gu et al., 2016; Iadanza et al., 2016; Noinaj et al., 2014). To explain the requirement for BamA β seam opening, we recently performed an *in vivo* crosslinking study that captured a snapshot of the folding process in which the β signal strand of an incompletely folded β barrel was fully paired with BamA β strand 1 (β1) via an antiparallel inter-strand interface to form a remarkable "hybrid-barrel" intermediate folding state (Doyle and Bernstein, 2019). In that study, the opposing interface between the C terminus of BamA and the N terminus of the β barrel substrate was extremely dynamic, which suggests the presence of multiple transition states during the assembly process (Doyle and Bernstein, 2019). A 4 Å resolution cryo-electron microscopy (cryo-EM) structure of BAM engaged during the folding of an assembly-deficient BamA deletion mutant (BamA$_{\Delta L1}$) in detergent micelles also showed BamAβ1 bound to the C terminus of BamA$_{\Delta L1}$ to form a late-stage hybrid-barrel intermediate (Tomasek et al., 2020). Although the structure might depict a similar stage of β barrel folding, the BAM-BamA$_{\Delta L1}$ interface is twisted and results in a "W-shaped" structure that is not fully hybridized (Tomasek et al., 2020). Due to the non-canonical final folded structure and unusual β seam dynamics of BamA, it is likely that this intermediate state is specific to the assembly of BamA and does not occur during the folding of typical OMPs. Moreover, the BAM-BamA$_{\Delta L1}$ structure did not show how BAM recognizes the terminal phenylalanine in β signals or reveal the dynamics of the folding process that results in the late hybrid-barrel state.

Mostly because the reconstitution of the native OM *in vitro* remains a significant technical challenge, the role of the membrane itself in OMP folding has often been neglected. Unlike other biological membranes, the bacterial OM is an asymmetric bilayer that is composed of a glycolipid known as lipopolysaccharide (LPS) in the outer leaflet and phospholipids in the inner leaflet (Horne et al., 2020). The concentration of OMPs within the OM is also extremely high and has been estimated to account for over 50% of the OM volume (Horne et al., 2020; Jarosławski et al., 2009). Because the interactions between densely packed β barrels and LPS molecules result in a rigid structure in which protein diffusion is low (Rassam et al., 2015; Rojas et al., 2018; Ursell et al., 2012), the mechanism by which β barrels are folded into the OM is even more puzzling. A recent study showed that the BAM lipoproteins can alter membrane fluidity (albeit in synthetic bilayers) and thereby potentially facilitate β barrel integration (White et al., 2021). Intriguing molecular dynamics (MD) simulations have also raised the possibility that the distinctive "wedge-shaped" aromatic girdles of the BamA β barrel might thin the OM to reduce the energy required for assembly (Liu and Gumbart, 2020; Noinaj et al., 2013).

Here, we examined the folding of a model *E. coli* O157:H7 OMP (EspP) that contains a stably closed (i.e., fully hydrogen-bonded) β seam, a typical 12-stranded β barrel, and a canonical β signal (Barnard et al., 2007; Wang et al., 2021). By using single-particle cryo-EM to analyze an assembly-arrested form of the protein associated with BAM in native nanodiscs that contain components directly extracted from the bacterial OM (unlike previous structural studies that used detergent or nanodiscs with synthetic phospholipids), we were able to visualize multiple intermediate stages of β barrel folding. Unlike BamA$_{\Delta L1}$, EspP forms an intermediate structure in which its conserved β signal is fully hybridized with BamA to form a "B-shaped" hybrid-barrel. The critical phenylalanine in the EspP β signal is positioned on BAM within an unusual binding pocket that interfaces with the OM to correctly orient the new OMP during folding. We also obtained direct evidence that BAM alters the structure of the OM via membrane thinning and interfacial LPS/lipid stabilization. Remarkably, in some of the intermediate hybrid-barrel structures, the OM around the folding EspP β barrel was deflected at an angle relative to the plane of the OM around BamA. This phenomenon is unlike any known membrane-bending process (Prinz and Hinshaw, 2009). Our structural data, combined with the results of *in vivo* experiments in which β barrel assembly was monitored during transient modulation of OM tension, led us to a model in which BAM utilizes the intrinsic structure of β barrels and the mechanical properties of the OM itself to accelerate the final stages of OMP folding.

RESULTS

Structure of BAM folding a β barrel substrate in native OM nanodiscs

To isolate an active form of BAM that is engaged in catalyzing the folding of a new β barrel, we utilized a derivative of EspP ($^{\text{MBP-76}}$EspP) whose assembly is arrested at a late stage while it is still bound to BAM (Doyle and Bernstein, 2019). EspP is a member of the autotransporter family of OMPs that consist of a C-terminal β barrel and an N-terminal extracellular ("passenger") domain that is translocated across the OM by BamA (Doyle and Bernstein, 2021). To construct $^{\text{MBP-76}}$EspP, we replaced most of the passenger domain with maltose binding protein (MBP), a protein that folds rapidly in the periplasm and, consequently, prevents translocation due to the size constraints of the channel. Because translocation must be completed before BamA releases a fully folded EspP β barrel (Ieva and Bernstein, 2009; Ieva et al., 2011), $^{\text{MBP-76}}$EspP remains bound to BamA in a hybrid-barrel state in which the β signal is fully hybridized to BamAβ1 (Doyle and Bernstein, 2019). Importantly, BAM-$^{\text{MBP-76}}$EspP co-complexes represent *bona fide* folding intermediates because β barrel folding can be completed when the MBP-containing portion of $^{\text{MBP-76}}$EspP is removed by proteolysis (Doyle and Bernstein, 2019). To increase stability during purification, we used an *E. coli* strain transformed with plasmids expressing $^{\text{His}}$BamA$_{\text{S425C}}$BCDE and $^{\text{MBP-76}}$EspP$_{\text{S1299C}}$ and generated a disulfide bond between two residues in BamAβ1 and the EspP β signal that is proximal during the natural hybrid-barrel assembly step *in vivo* (Doyle and Bernstein, 2019).

To more faithfully reconstitute an OM environment than previous structural studies on BAM (and other OMPs), we used a detergent-free system involving styrene-maleic acid (SMA) copolymers to directly solubilize and isolate BAM-$^{MBP-76}$EspP co-complexes into native nanodiscs. Based on structural studies on α-helical membrane proteins, our BAM-$^{MBP-76}$EspP OM nanodiscs likely contain locally derived phospholipids and LPS (Lee et al., 2016; Sun et al., 2018). Purified BAM-$^{MBP-76}$EspP OM nanodiscs contained lipoproteins in the correct stoichiometry (Figure 1A). Tandem mass spectrometry (MS/MS) and immunoblotting also validated the presence of expected lipids including LPS, phosphatidylethanolamine (PE), phosphatidylglycerol (PG), and cardiolipin (CL) as well as multiple forms of lysophosphatidylethanolamine (LPE), a lipid that appears to have membrane remodeling properties (Figure S1K; Table S1; Zheng et al., 2017). The BamA-$^{MBP-76}$EspP hybrid-barrel exhibited an intrinsic feature of β barrels, when examined by SDS-PAGE, in that in the absence of heat it was resistant to unfolding by SDS and migrated more rapidly (Doyle and Bernstein, 2019). Furthermore, the rapidly migrating BamA-$^{MBP-76}$EspP hybrid-barrels also ran as diffuse bands (Figure 1A, left lane) that presumably resulted from dynamic interactions between the EspP β barrel N-terminal strand and BamA C-terminal strands that were previously observed during folding *in vivo* (Doyle and Bernstein, 2019).

A high-resolution structure of the purified BAM-$^{MBP-76}$EspP OM nanodiscs was solved to a global resolution of 3.6 Å by single-particle cryo-EM (Figures 1B, S1, and S2). The structure revealed BamA in an overall outward-open conformation with BamAβ1 associated with the EspP β signal to form a hybrid-barrel intermediate folding state (Figure 1B). In this map, only four C-terminal β strands of the actively folding EspP β barrel were clearly resolved. These β strands extended into a low-resolution region within the OM-nanodisc that likely represents the remainder of the amphipathic EspP β barrel, creating a border between the membrane and an internal space devoid of EM density (Figure 1C). The low resolution of the EspP β barrel N terminus suggests that this portion of the protein transitions between multiple highly dynamic folding substates, a notion consistent with the previously observed dynamic interface between the EspP β barrel N terminus and BamAβ15/16 mentioned above (Doyle and Bernstein, 2019).

Comparison of our structure to the BAM-BamA$_{\Delta L1}$ structure (Tomasek and Kahne, 2021) showed striking differences. Whereas the hybridization interface between BAM and the BamA$_{\Delta L1}$ mutant is twisted to form a W-shaped hybrid-barrel, the BamA-EspP hybridization interface forms a continuous flat β sheet (Figure 1D). This difference stems from the ability of BamAβ1/2 to flex and tilt in the membrane and suggests a mechanism by which BamA can accommodate the folding and integration of different β barrel substrates. In the BAM-$^{MBP-76}$EspP structure, BamA POTRA3 and BamB (through its association with POTRA3) are also positioned closer to the membrane (Figures 1D and S1). Conformational changes localized near the N-terminal α helices of BamD likewise result in a shift toward the membrane with α helix 2 interfacing with the outer side of the periplasmic turns of the folding EspP β barrel (Figures 1D and S1). This overall conformation contrasts with the BAM-BamA$_{\Delta L1}$ structure in which BamD is positioned beneath the lumen of BamA$_{\Delta L1}$. To test whether BamD can interact with the periplasmic turns of EspP during a hybrid-barrel stage of assembly *in vivo*, BAM containing a BamD$_{R49C}$ subunit was co-expressed in *E. coli* with $^{MBP-76}$EspP$_{D1218C}$, and cells were treated with a thiol-specific disulfide-oxidation catalyst. Consistent with our structure, strong disulfide crosslinking between $^{MBP-76}$EspP$_{D1218C}$ and BamD$_{R49C}$ was observed after chemical oxidation but not in the control strain expressing a wild-type (WT) BamD allele (Figure 1E). The observation that crosslinking plateaued at ~40% suggests the presence of additional substates with alternate conformations of EspP relative to BamD (Figures 1E and S1). A higher than expected level of spontaneous crosslinking (~10%, Figure 1E, Ox−) also indicated the existence of a stage in which EspP interacts with BamD very stably. Interestingly, EspP D1218 is close to a recently discovered conserved "-5-signal" in strand 8 that was shown to interact with BamD just downstream of residue R49 in an *in vitro* assembly reaction (Germany et al., 2021).

Strikingly, in the BAM-$^{MBP-76}$EspP structure we were able to clearly resolve the conserved residues of the canonical β signal of EspP (Figures 1B and 1F). The terminal EspP β signal residue (F1300) is oriented over BamAβ1 in a space created by BamA$_{G424}$ that forms a structural arrangement reminiscent of stabilizing intra-barrel "mortise-tenon joints" (Figures 1F and 1G; Leyton et al., 2014). G424 is conserved in all Gram-negative bacteria except the *Bacteroides*, and the mutation of this residue strongly impairs the growth of *E. coli* (Kaur et al., 2021; Xiao et al., 2021). BAM interacts with F1300 via BamA T423, G424, F426, and Q446 within an unusual membrane-facing hydrophobic pocket (Figure 1F). Nevertheless, the β signal binding pocket is not totally filled. This property might enable BAM to accommodate the less common subset of OMPs that have β signals terminated by tryptophan or tyrosine instead of phenylalanine. The conserved β signal residue at the -3 position of EspP (Y1298) interacts with BamD L124 (a residue that varies among BamD homologs) and is oriented into the membrane plane at a depth corresponding to the aromatic girdles of fully folded canonical β barrels (Figure 1F). Overall, the structure suggests that BAM binds to β signals to correctly orient the C-terminal strands of new OMPs into the OM during the folding process and is consistent with our previously reported *in vivo* crosslinking results (Doyle and Bernstein, 2019). Interestingly, darobactin (a recently discovered BAM inhibitor) (Imai et al., 2019) and the β signal interact with BamAβ1 in a highly similar way; like EspP F1300, the terminal phenylalanine of the darobactin peptide is positioned over BamA$_{G424}$ (Kaur et al., 2021; Figures 1G and S1). Therefore, our structure not only provides the structural basis for native OMP β signal binding by BAM during assembly, but also definitively shows that darobactin is a competitive inhibitor of OMP substrate recognition and thereby helps to explain its bacteriocidal potency.

An important aspect of our study is that by solving the structure of BAM-$^{MBP-76}$EspP within native nanodiscs that harbor local OM lipids captured during solubilization, we can consider the role of the OM in OMP assembly. In our BAM-$^{MBP-76}$EspP

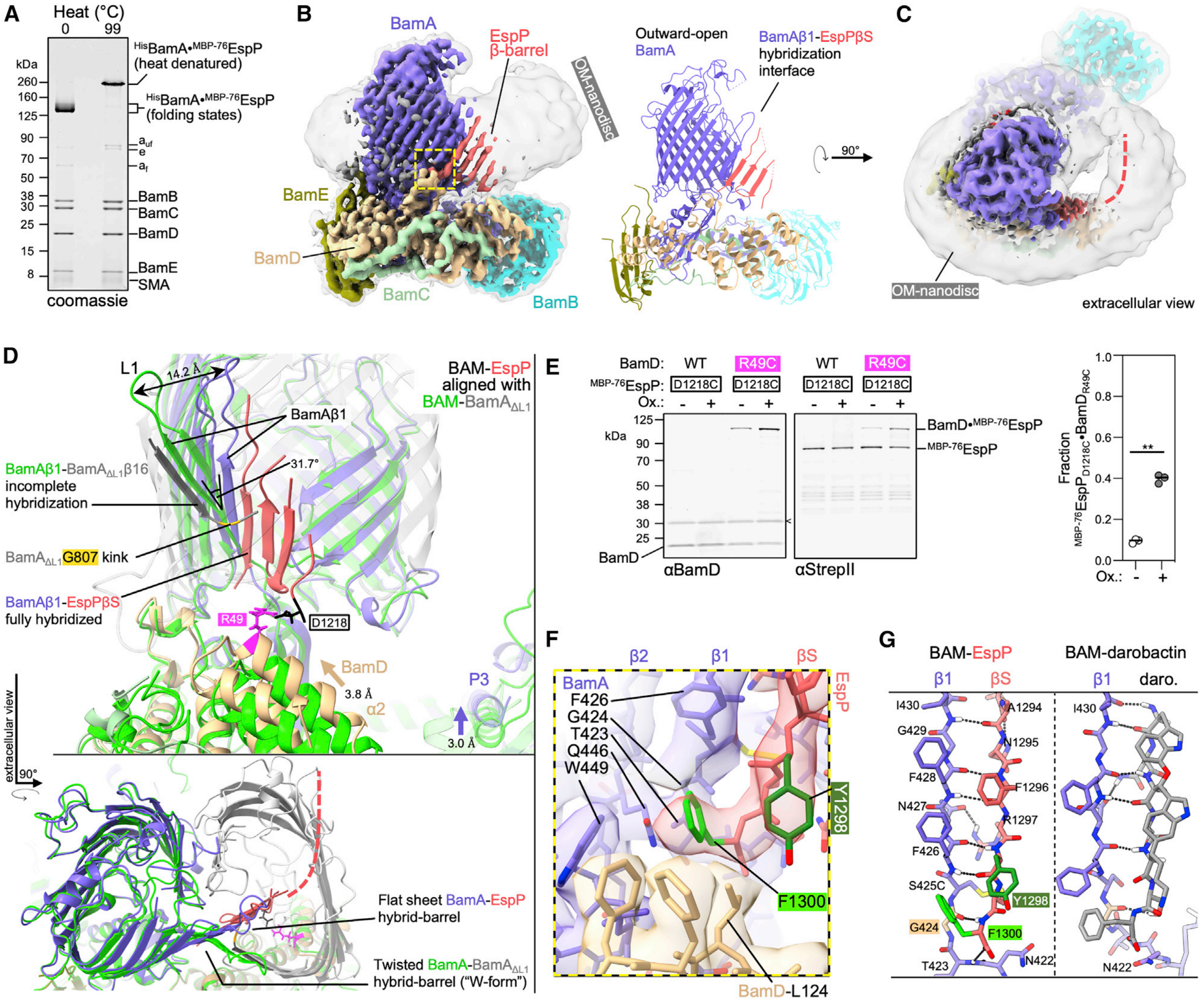

Figure 1. BAM binds the conserved OMP β signal to form a flat hybrid β sheet in the OM

(A) Heat denatured (99°C) or unheated BAM-$^{MBP-76}$EspP OM nanodiscs were resolved by cold-SDS-PAGE. BamA$_{S425C}$ and $^{MBP-76}$EspP$_{S1299C}$ were disulfide-bonded. Unoxidized $^{MBP-76}$EspP (E), BamA folded (a_f) and unfolded (a_{uf}) species, and SMA copolymers are indicated.

(B) High-resolution cryo-EM map (left, 3.6 Å average) and model of BAM-$^{MBP-76}$EspP (right). Map colored by subunit. Local resolution filtered map at a lower threshold level (left, transparent gray) shows OM-disc boundary. BamA is in an outward-open conformation and hybridized to the EspP β signal (βS) via BamA β strand 1 (B1) (yellow box).

(C) Extracellular top view of map shown in (B). Dashed line indicates the likely location of the remainder of the EspP β barrel.

(D) Substrate-specific intermediate folding states during assembly of EspP and BamA$_{\Delta L1}$ β barrels. Structure of BAM-BamA$_{\Delta L1}$ hybrid-barrel intermediate state in detergent (PDB: 6V05; BAM, green; BamA$_{\Delta L1}$, transparent gray) is aligned with the BAM-$^{MBP-76}$EspP structure (subunit colors as in [C]). The final strand of BamA$_{\Delta L1}$ is not fully hybridized with BamAβ1 (kink at BamA$_{G807}$, yellow), whereas the conserved EspP β signal strand is fully hybridized with BamAβ1. A 31.7° difference in BamAβ1 tilt angle (axis residues 427–434 alpha carbons [αC]) coincides with either "flat-sheet" (BamA-EspP) or twisted "W-shaped" (BamA-BamA$_{\Delta L1}$) hybrid-barrel assembly intermediates. BamA POTRA3 (P3) and BamD α helix 2 (A2) are denoted.

(E) *E. coli* expressing ^{His}BamABCDE (or ^{His}BamABCD$_{R49C}$E) and $^{MBP-76}$EspP$_{D1218C}$ (residues mutated to cysteine indicated in [D]) were mock treated (Ox−) or treated with 4-DPS (Ox+), and BamD·$^{MBP-76}$EspP crosslinks were identified by double-immunoblotting with αBamD and αStrepII (StrepII-tag at $^{MBP-76}$EspP N terminus) antibodies (n = 3). Non-specific band is denoted (<). The graph shows the fraction of crosslinked BamD·$^{MBP-76}$EspP (line at median, two-tailed paired t test: p = 0.0019 [**]).

(F) β signal terminal residue binding pocket (magnified yellow box in [B]). Highly conserved Y1298 (-3) and F1300 (-1) residues are indicated.

(G) Comparison of BamAβ1-EspP β signal strand and BamAβ1-darobactin (PDB: 7NRI) interactions. In both cases F(-1) is positioned over the space created by BamA$_{G424}$ (tan). Dotted lines denote H-bonds.

See also Figure S1.

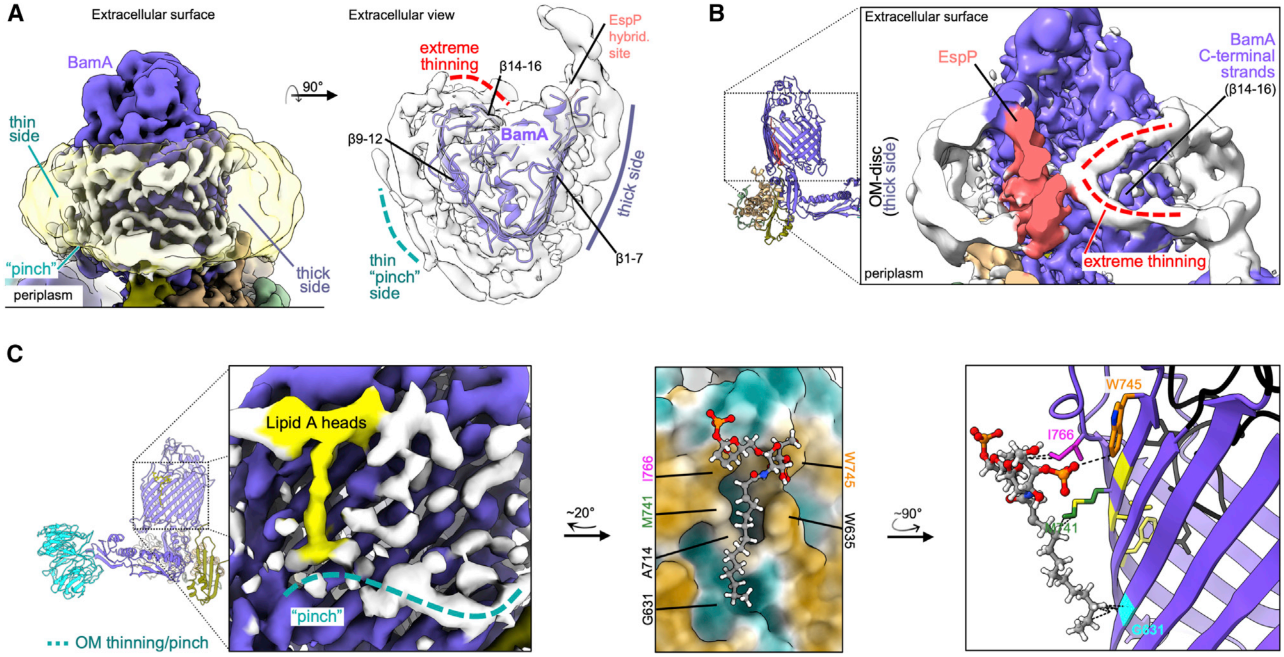

Figure 2. OM thinning and lipid/LPS ordering during OMP folding

(A) Left, side view of BAM-$^{MBP\text{-}76}$EspP OM-nanodisc showing both thin and thick membrane sides around BamA (local resolution filtered map to show protein [colored] and membrane [white] features and at a lower threshold [clear yellow] to show disc boundary). Right, extracellular view of map showing repeated pattern in the OM disc indicative of outer leaflet interfacial lipid A head groups.

(B) Cut-away view of BAM-$^{MBP\text{-}76}$EspP map (rotated ∼180° from A, left) showing extreme thinning (red dashed lines, as also indicated in [A]) of OM-disc density that coincides with BamAβ14-16.

(C) Left, BAM-$^{MBP\text{-}76}$EspP map shows density (yellow) consistent with a lipid A head group and a stabilized acyl chain on the thin side of the BamA β barrel (teal dashed line). Middle, modeled lipid A coincides with a groove on the side of BamA. BamA surface colored by high hydrophobicity (brown) to low hydrophobicity (teal). Right, another angle showing putative secondary interactions (dashed lines) between lipid A and BamA residues. Conserved BamA motif FxDxG (yellow) that interacts with loop 6 (black) on the inside of the β barrel are shown.

See also Figure S1.

map, we observed a repetitive pattern of stabilized density circling the BamA β barrel at the expected location and size of outer leaflet LPS lipid A head groups and clear boundaries that likely represent density for inner leaflet phospholipid head groups (Figure 2A). It has been postulated that BamA locally thins the OM to decrease the energetic penalty of OMP integration (Liu and Gumbart, 2020; Noinaj et al., 2013). Consistent with this hypothesis, our map suggests that the membrane near the N-terminal half of the BamA β barrel (∼β1-7) is thicker than the side of the OM nanodiscs near strands β9-12, which appeared to thin to a "pinch-point" (Figures 2A–2C). These patterns coincidently match recent MD simulations that predict thickening/thinning patterns around BamA at the same locations (Liu and Gumbart, 2020). The map also suggests even more extreme membrane thinning near BamAβ14-16 (Figure 2B). At the location of the pinch-point, we also observed striking density that likely corresponds to a lipid A moiety with a single stabilized acyl chain (the other lipid A acyl chains are presumably dynamic) (Figure 2C). The stabilized acyl chain lies within a groove alongside BamAβ11-12 that is created by the lipid-facing residues G631 and A714 (a moderately well-conserved amino acid). Because the change in membrane thickness and acyl chain stabilization patterns observed in the high-resolution BAM-$^{MBP\text{-}76}$EspP structure were likewise observed in our subsequent independent BAM-$^{MBP\text{-}76}$EspP reconstructions (see below and Figure S1L), they are likely valid structural features. Based on the occurrence of the two phenomena at the same location, it is possible that stabilization of the acyl chain on the C-terminal side of BamA helps to mediate the process of membrane thinning.

The BAM, the OM, and the incoming OMP each undergo major structural transitions during β barrel folding

Although our BAM-$^{MBP\text{-}76}$EspP map has a higher global resolution than the previously solved BAM-BamA$_{\Delta L1}$ structure, the local resolution was poor in the area corresponding to the N-terminal portion of the EspP β barrel and low for BamA P3/BamB and the N terminus of BamD (Figure 3A), presumably due to dynamicity in these regions. During the processing of ∼1.2 M high-quality particles to generate the map (STAR Methods, strategy 1), we noticed specific low-resolution classes that appeared to have alternate conformations in these areas and wondered whether a more conservative processing strategy could improve their local resolution (at the expense of global resolution). To that end, we reprocessed the particle pool into six classes yielding maps with global resolutions between 4.2–4.5 Å (Figures 3B

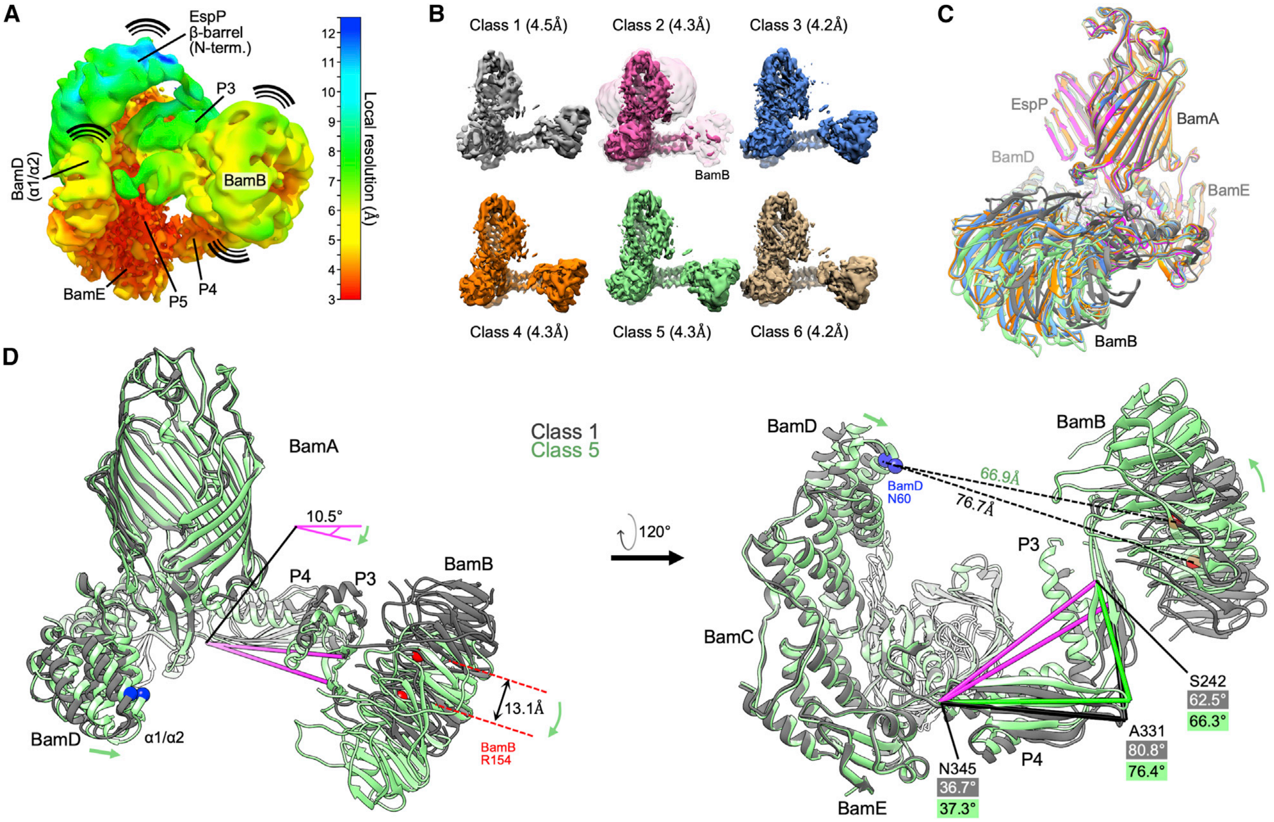

Figure 3. Conformational changes of BAM periplasmic components during OMP folding

(A) The BAM-$^{MBP-76}$EspP high-resolution map (shown in Figure 1B) filtered and colored by local resolution. Low-resolution components (e.g., EspP β barrel N terminus, BamB, and BamA P3) are conformationally dynamic. High-resolution components (e.g., BamE and P5) are structurally stable.

(B) Structurally diverse cryo-EM maps of BAM-$^{MBP-76}$EspP. Maps filtered by local resolution. Class 2 also shown at a lower threshold level (clear pink) to show BamB.

(C) Models of BAM-$^{MBP-76}$EspP Classes 1–6 were aligned (on P5 residues Y348-R421). View shows large conformational variability in BamB positioning. Colors as in (B).

(D) Classes 1 and 5 aligned as in (C). Conformational changes are depicted by green arrows. Axis (pink) from BamA S242 (P3) to N345 (hinge region between P4 and P5) α carbons flexes by 10.5° among classes. Changes in the angles between S242, A331, and N345 also show flexing between P3 and P4 among classes. See also Figure S3.

and S3; STAR Methods, strategy 2). The conformation of the BamA β barrel is essentially identical in all the structures (Figure 3C). Classes 3, 4, and 6 are similar to the original high-resolution structure but contain slight changes in the position of BamB and the N terminus of BamD. The density of BamB is poor in class 2 (although it is visible at lower thresholds), presumably because it is highly dynamic (Figure 3B). Indeed, between all the classes the largest overall BAM conformational changes are in the positioning of BamB (Figure 3C; Video S1). Classes 1 and 5 represent extremes in which the BamA POTRA domains and BamD move closer or farther away from each other (Figure 3D). Concomitantly, BamA P3 moves toward or away from the membrane, and consequently, the position of BamB changes very significantly. Together, these reconstructions show that BAM periplasmic components undergo large conformational changes during the late stages of OMP folding that are reminiscent of their structural heterogeneity in apo-BAM (Iadanza et al., 2020).

The simple classification approach did not improve the maps in the region corresponding to the folding EspP β barrel. To better resolve the intermediate folding states, we subtracted the signals for BamB, BamA P3, and the BamD N terminus from our particles and conducted focused classification on the remaining complex (STAR Methods, strategy 3). We reasoned that removing these dominant sources of structural heterogeneity would improve alignment of the structural substates of the EspP β barrel N terminus during the hybrid-barrel stage that were predicted from our *in vivo* experiments (Doyle and Bernstein, 2019). Consistent with our hypothesis, we were able to generate multiple reconstructions of hybrid-barrel substates using this processing strategy (Figures 4 and S3). In one structure that we designate the "open-sheet" (OS)-state (Figure 4A), the EspP β barrel is observed as a remarkable membrane-integrated open β sheet with its C terminus hybridized to BamA. In this state, the OM-nanodisc is deflected around the EspP transmembrane β sheet at an angle that results in a mismatch of the membrane plane around BamA (Figure 4A). In the "intermediate-open" (IO)-state (Figure 4B), the reconstructed BAM components are essentially identical to the OS-state with both

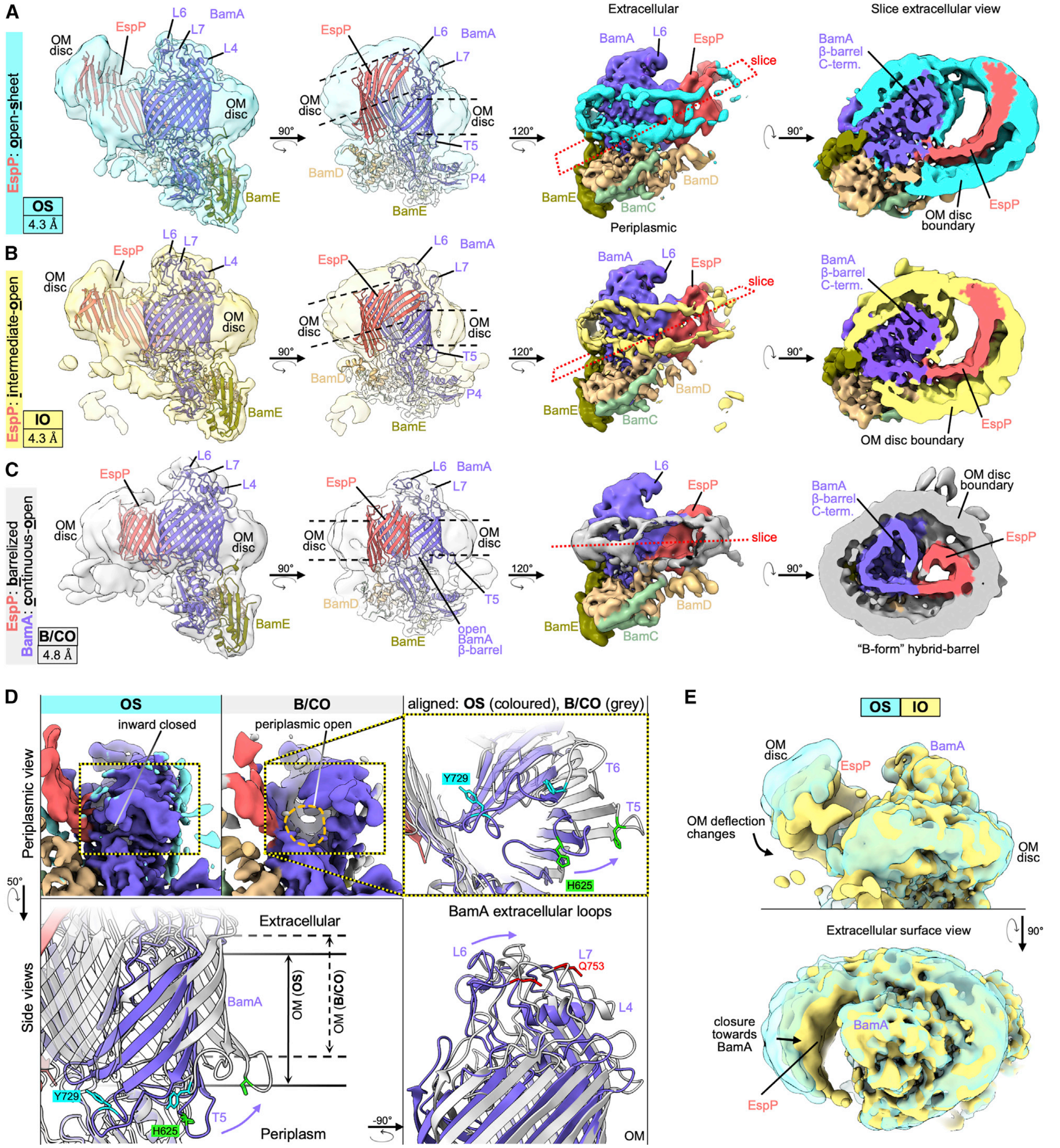

Figure 4. Focused classification reveals a continuous-open BamA β barrel and multiple hybrid-barrel substates during EspP folding

(A–C) Focused classification of particles with subtracted signals of dynamic periplasmic components (BamD N-term, P3, and BamB) identified three distinct BamA-EspP hybrid-barrel conformations: EspP "open-sheet" (OS [A], OM disc in cyan), EspP "intermediate-open" (IO [B], OM disc in yellow), and EspP "barrelized"/BamA "continuous-open" (B/CO [C], OM disc in light gray). Map resolutions noted at bottom left. Dashed lines in mid-left views indicate in-plane or deflected bilayer angles. Right views, maps are colored by subunit. Far-right, slices across the hybrid-barrels (slice planes depicted mid-right) show expanded hybrid-barrels for OS- and IO-state and a "B-shaped" hybrid-barrel for the B/CO-state. Maps are filtered by local resolution.

(D) Identification of a novel BamA conformation during OMP assembly. The B/CO class exhibits the BamA β barrel in an expanded conformation similar to outward-open conformations but with a periplasmic opening (compare maps top left and middle, periplasmic view). In top-right and bottom panels, models of OS

(legend continued on next page)

structures showing BamA in an outward-open conformation. However, compared with the OS-state, in the IO-state the EspP transmembrane β sheet is folded closer to BamA, and the observed membrane deflection is less extreme. In a third structure that we call the "barrelized/continuous-open" (B/CO)-state, we observed a "B-shaped" BamA-EspP hybrid-barrel but, unlike the other states, no obvious membrane deflection (Figure 4C). This state presumably represents a very late stage of EspP assembly in which the β barrel structure is nearly complete. In the B/CO-state, BAM is observed in a conformation (that has not been observed in any previously published BamA structures) in which the C-terminal half of the BamA β barrel is expanded away from the N terminus and repositioned higher in the membrane plane so that its surface loops (including L4, 6, and 7) are shifted away from the EspP β barrel (Figures 4D and S4). The result is a BamA structure reminiscent of outward-open states but with an opening that creates a continuous channel through the OM-nanodisc (Figure 4D). This structure may represent a stage prior to the release of the EspP β barrel that we have recently observed *in vivo* in which the BamA β barrel facilitates secretion of the EspP passenger domain (Doyle and Bernstein, 2021).

Antagonism between the intrinsic structure of OMPs and OM tension drives late folding

Although we cannot definitively order the three hybrid-barrel substates in a temporal sequence, because they are derived from the same sample, a simple interpretation of the data is that the OS-state represents an early stage of folding following the membrane integration of the EspP β sheet, the IO-state represents a slightly later stage in which the EspP β sheet folds toward BamA, and the B/CO-state represents a relatively late stage in which the β sheet folds into a barrel-like structure (see Video S2). It is notable that the changes in EspP folding between OS and IO states were not associated with major structural changes in BamA. Furthermore, the extreme nature of the expanded EspP β sheet and membrane deflections in the OS and IO states were very surprising and warranted an explanation that places these states in the context of folding within the native OM.

To rationalize our findings, we conceptualized a new model of the late stages of OMP assembly by considering the intrinsic structure of transmembrane β barrels and the rigidity of the OM. OMP β strands are tilted by ~45° from the barrel-axis (Schulz, 2000) and, due to the presence of aromatic girdles and other membrane-facing hydrophobic residues in β barrel transmembrane β sheets, fully folded OMPs are often slightly tilted in the OM (Lomize et al., 2012). We calculated the membrane orientations of solved *E. coli* β barrels and then illustrated them as open β sheets while maintaining their β signals in their calculated positions relative to the OM plane (Figures 5A and S5A). The result is a mismatch in which the N-terminal transmembrane β strands would not reside in the normal OM plane but would instead deflect the membrane. Consistent with this hypothetical scenario, the OS- and IO-state structures capture EspP as an incompletely folded open β sheet at an angle relative to the normal OM plane (Figures 4A, 4B, 5B, and S5B). Indeed, in all our structures we observe BamA bound to the EspP β signal at an even higher angle than at which the β signal is situated after EspP is completely folded (~64.6° versus 58°; Figures 5A, 5B, and S5B). Furthermore, the difference between the angle of the β signal of some OMPs when bound to BamA as an open β sheet versus the fully folded form may be even greater (Figure S5A; see PgaA). The outward-open BamA conformation might therefore create a highly antagonistic scenario between the normal OM plane and the intrinsic structure of incompletely folded β barrels that deflects the membrane (Figures 4A, 4B, and 5B). This scenario, however, should be considered in light of the finding that unlike other biological membranes, the OM forms a very rigid structure (stiffer than the peptidoglycan cell wall) due to interactions between LPS molecules, the high OMP density, and the stiffness of OMPs themselves (Horne et al., 2020; Jarosławski et al., 2009; Lessen et al., 2018; Rojas et al., 2018). Indeed, due to its rigidity, the OM has been observed to function as a "spring" that undergoes compressive changes during osmotic shock (Rojas et al., 2018). Although stretching and compressive forces appear to be globally equalized across the *E. coli* OM during steady-state growth, our model predicts that the intrinsic structure of hybrid-barrel deflected β sheets (Figures 4A and 4B) would be countered by the intrinsic local tensile forces of the OM to help drive the closure of β barrels (Figure 5B).

To test our model *in vivo*, we expressed $^{\text{MBP-76}}$EspP alongside BAM in *E. coli* to create a pool of BamA-$^{\text{MBP-76}}$EspP hybrid-barrels in the OM and subsequently monitored late-stage β barrel folding kinetics during modification of OM tension via osmotic shock. As mentioned earlier, the assembly of $^{\text{MBP-76}}$EspP can be restarted from the hybrid-barrel stage by adding a protease that removes the MBP portion responsible for arresting assembly. Completion of folding can then be assessed by monitoring the auto-catalytic cleavage of the passenger domain that occurs after it is fully secreted and the β barrel reaches its native conformation (Dautin et al., 2007; Ieva and Bernstein, 2009). As observed previously (Doyle and Bernstein, 2019, 2021), adding proteinase K (PK) to bacteria suspended in isotonic LB medium (i.e., the same medium in which they were grown) released ~30 kDa C-terminal EspP fragments from the fusion protein that were rapidly converted into folded ~27 kDa β barrels and a peptide derived from the passenger domain that was not detected (Figure 5C, top left and black curves). However, when bacteria were exchanged into a hypertonic LB medium to relax the OM (Rojas et al., 2018) prior to the addition of PK, the incompletely folded C-terminal EspP fragments accumulated, and the rate of their conversion to fully folded β barrels was significantly reduced (Figure 5C, bottom left and blue curves). Although the β

and B/CO states are aligned (on P5 residues Y348-R421) showing that the C-terminal half of the BamA β barrel (β8-16) both expands and shifts away from the periplasm. The expansion coincides with extracellular loops (L4, L6, and L7) moving away from the hybridization interface. Residues H625, Y729, and Q753 (L7) are shown to emphasize the structural differences between each state (αC repositioned by 14.5, 16.2, and 9.8 Å, respectively). Turns T5 and T6 are also denoted.
(E) Overlay of OS and IO maps (filtered by local resolution) shows changes in the degree of OM-bilayer deflection and closure in the EspP β sheet region.
See also Figures S3 and S4.

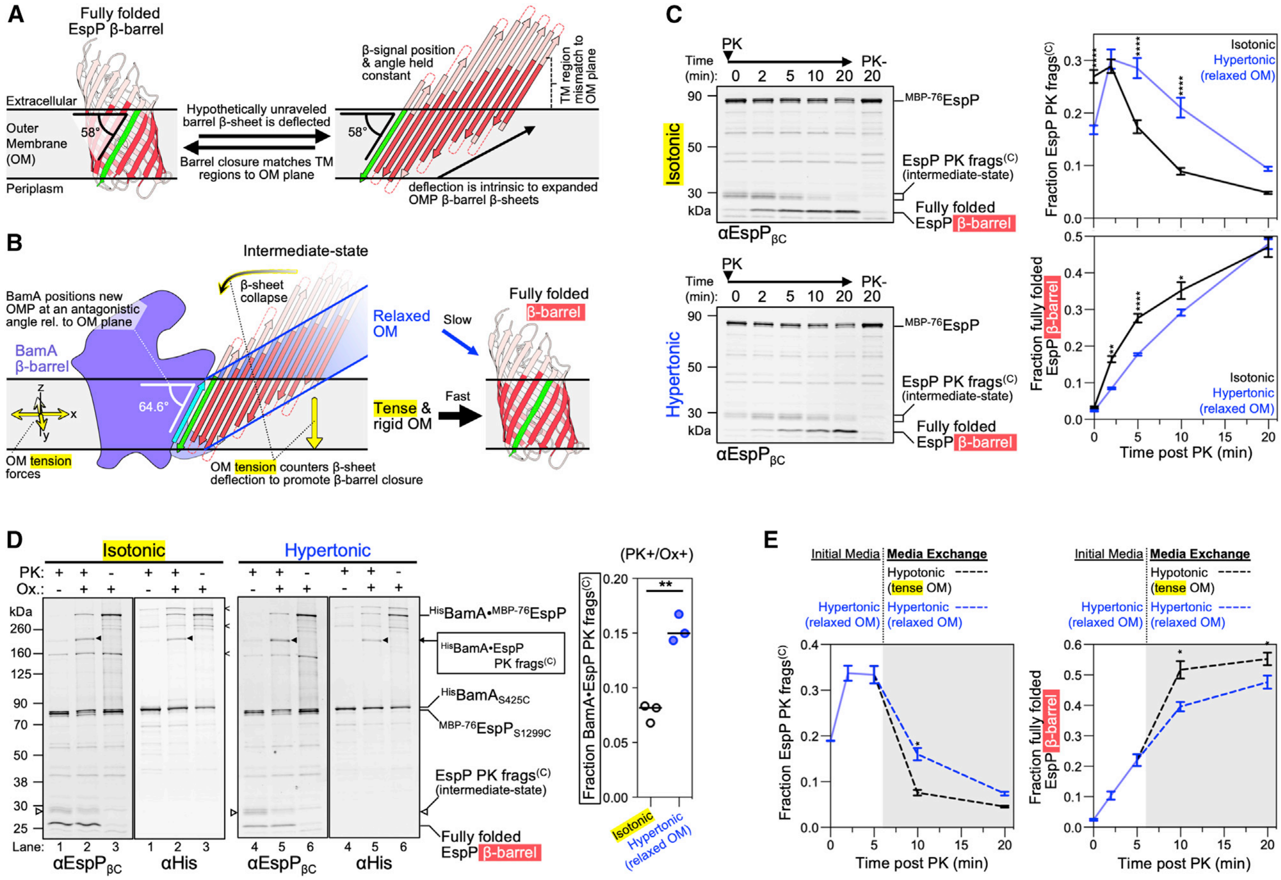

Figure 5. OM tension accelerates transmembrane β barrel folding

(A) Hypothetically unraveled EspP β barrel with the position of the conserved β signal strand (green) held constant to its angular membrane orientation when fully folded (58° for EspP, membrane plane calculated using OPM server) (Lomize et al., 2012) showing intrinsic mismatch between the membrane plane and the transmembrane portion of β strands (red). Loops and turns are not drawn to scale.

(B) EspP β sheet as in (A) except model depicted with the experimentally determined angle (using the BAM-$^{MBP\text{-}76}$EspP structure) of EspP β signal relative to the membrane when hybridized to BamAβ1 (cyan). The model predicts that the intrinsic tension forces of the rigid OM aid β barrel folding by countering the intrinsic deflection of an incompletely folded expanded β sheet.

(C) *E. coli* expressing ^{His}BamABCDE and $^{MBP\text{-}76}$EspP were suspended in LB (isotonic control) or LB-sorbitol (hypertonic). β barrel folding was restarted from the hybrid-barrel stage by adding PK to release a C-terminal EspP fragment (frags$^{(C)}$). Fragment conversion to a completely folded β barrel, after PK addition, was monitored by immunoblotting with an antiserum against the C terminus of EspP (αEspP$_{\beta C}$). Left, representative blots. Right, mean fraction of the EspP PK fragment (top) or converted into a folded β barrel (bottom) (±SEM, n = 4).

(D) *E. coli* expressing ^{His}BamA$_{S425C}$BCDE and $^{MBP\text{-}76}$EspP$_{S1299C}$ were grown and treated as in (C) except that samples at 5 min post-PK were mock treated (Ox−) or treated with 4-DPS (Ox+), and ^{His}BamA·$^{MBP\text{-}76}$EspP crosslinks were identified by double-immunoblotting with αEspP$_{\beta C}$ and αHis antibodies (n = 3). Non-specific crosslinks are denoted (<). Right, fraction of crosslinked BamA·$^{MBP\text{-}76}$EspP C-terminal PK fragment detected with αEspP$_{\beta C}$ (line at median, two-tailed paired t test: $p = 0.0038$ [**]).

(E) Bacteria were treated as in (C) except that after 5 min of PK treatment, the media was exchanged for either LB-sorbitol (hypertonic) or LB (hypotonic) (gray plot area). Plots are mean fraction (±SEM, n = 3). For (C and E), two-way repeated measures ANOVA (Šídák's tests) were performed $^*p < 0.05$, $^{**}p < 0.01$, and $^{****}p < 0.0001$.

See also Figure S5.

barrel assembly delay under hypertonic conditions was most notable at 5 min after PK addition, by 20 min there was no difference in the level of folded β barrel between the two conditions (Figure 5C). This observation strongly suggests that the delay was due to an energetic effect and that the hypertonic conditions did not simply block completion of β barrel folding. It should be noted that the osmotic shock neither disrupted the integrity of the OM nor led to a change in the level of SurA (via the induction of the σ^E stress response; see Rhodius et al., 2005) under our experimental conditions (Figures S5C and S5D). To directly pinpoint the delay to the period that follows the formation of the hybrid-barrel but that precedes the completion of EspP β barrel folding, the experiment was repeated using the strain expressing ^{His}BamA$_{S425C}$BCDE and $^{MBP\text{-}76}$EspP$_{S1299C}$. Samples were treated with PK for 5 min (or mock treated) and oxidized to promote disulfide crosslinking as described above. Consistent with previous results (Doyle and Bernstein, 2019), strong crosslinks between BamAβ1 and the $^{MBP\text{-}76}$EspP β signal were detected in oxidized samples without PK treatment (Figure 5D, lanes 3 and 6). In samples that were both oxidized and PK treated, the incompletely folded EspP C-terminal fragments were likewise crosslinked to BamA (Figure 5D, lanes 2 and 5, black arrows). These results confirm that hypertonic conditions do not interfere with the stability of the BamA-$^{\text{MBP-76}}$EspP assembly intermediate and pinpoint the delay to the period following the formation of the hybrid-barrel. Interestingly, EspP C-terminal PK fragments crosslinked to BamA at a statistically higher level under hypertonic conditions at the 5-min time point (Figure 5D, graph), suggesting that the association of incompletely folded EspP with BamA at the hybrid-barrel stage is prolonged when the OM is relaxed.

Finally, our model not only predicts that folding can be slowed by relaxing the OM, but that folding can be accelerated by increasing the OM tension. To test this idea, we repeated the assembly-restart experiment under hypertonic conditions, but 5 min after the addition of PK we exchanged the bacteria into an equivalent medium (control) or a hypotonic medium (to increase OM tension) and continued monitoring EspP β barrel folding. Consistent with our hypothesis, the EspP C-terminal fragments were converted more rapidly into folded β barrels when they were exchanged into a hypotonic medium (Figure 5E). This difference constitutes a substantial effect given that only a small fraction of incompletely folded EspP molecules remained to be tracked after the 5-min time point. Together, these results support a model in which BamA orients OMP substrates at an antagonistic angle to the OM to exploit the intrinsic tension of the OM as a useful driving force to accelerate β barrel folding (Figure 5B).

DISCUSSION

Although the first transmembrane β barrel structure was solved in 1990 (Weiss et al., 1990), how they are recognized, folded, and released into the bacterial OM in the absence of any known external energy sources remains poorly understood. In this work, we provide structural and biochemical evidence that help to explain all of these critical stages of OMP assembly. With respect to substrate recognition, our structural data reveal an unusual pocket in BAM that binds to the highly conserved C-terminal OMP β signal motif. During the hybrid-barrel intermediate stage, the terminal aromatic residue interacts with several adjacent BAM residues and is positioned over the space created by $\text{BamA}_{\text{G424}}$. The interaction resembles G-(F/Y/W)-based inter-strand mortise-tenon joints that are found within most OMPs and that provide structural stability (Leyton et al., 2014). The BamA-β signal interaction therefore constitutes an interesting inter-barrel mortise-tenon-like joint. The binding of BAM to the β signal provides an explanation for the finding that mutations of the terminal aromatic residue cause severe assembly defects and lead to OMP degradation *in vivo* (Gessmann et al., 2014; Lee et al., 2018; Wang et al., 2021). Presumably the mutations reduce the binding affinity of incoming OMPs to BAM, prevent their progression to the hybrid-barrel stage, and result in exposure to periplasmic proteases. Our discovery of this binding site may also facilitate the design of additional competitive inhibitors of β signal binding that, like darobactin, act as potent antibiotics against Gram-negative pathogens.

Our results provide evidence that the EspP C-terminal domain inserts into the OM as a β sheet and then folds into a β barrel in multiple steps. The structural data suggest that BAM binds to the β signal of EspP to form a flat hybridization interface and that this hybrid-barrel intermediate passes through several substantially different stages of folding (e.g., OS-, IO-, and B/CO-substates) resulting in a "B-shaped" hybrid-barrel. Ultimately, because the BamAβ1-EspP β signal backbone hydrogen-bond network is weaker than that of the β seam of fully folded EspP (Figure S5E), this configuration provides an energetically favorable mechanism for the release of the substrate into the lipid bilayer. Furthermore, we identified a substate in which BamA exists in a continuous-open conformation coinciding with a more barrel-like EspP structure (the B/CO-state). We recently showed that the unfolded passenger domain of $^{\text{MBP-76}}$EspP is secreted through the BamA β barrel lumen during a hybrid-barrel assembly stage *in vivo* (Doyle and Bernstein, 2021). We therefore speculate that the continuous opening in BamA observed in the B/CO-state may constitute a channel for the secretion of autotransporter passenger domains and extracellular segments of other OMPs. Despite the stability of $^{\text{MBP-76}}$EspP, we found that the passenger domain is extremely dynamic within the channel *in vivo* (Doyle and Bernstein, 2021), and this dynamicity may explain the lack of passenger domain density within the BamA pore in our reconstructions. Alternatively, the conformational changes observed in the surface loops of BamA in the B/CO-state relative to our other structures (e.g., L4, L6, and L7) may be required for the folding of β barrels more generally. Indeed, this finding may explain why the function of BAM is strongly inhibited when BamA L4 is bound by a bactericidal antibody Fab1 fragment that presumably prevents this conformational cycling (White et al., 2021). It is important to note that none of our reconstructions exhibited the twisted interface that results in a hybrid-barrel with a "W-shaped" cross-section observed in the BAM-$\text{BamA}_{\Delta\text{L1}}$ structure (Tomasek et al., 2020). Besides lacking a canonical C-terminal β signal, the $\text{BamA}_{\Delta\text{L1}}$ β barrel substrate has distinctive features such as an unstable β seam, extreme structural dynamics, and a kinked C terminus that likely causes the twisted hybridization interface observed during its assembly (Doerner and Sousa, 2017; Gu et al., 2016; Iadanza et al., 2016; Lundquist et al., 2018; Noinaj et al., 2013). Therefore, the W-form hybrid-barrels probably represent a late-stage intermediate that is specific to the assembly of BamA. Because the EspP β barrel follows the common architectural rules (e.g., it has a tightly closed β seam and a parallel aromatic girdle that is the same width as the OM; see Schulz, 2000) and possesses a canonical C-terminal β signal, we speculate that the majority of OMPs are folded through a late B-form hybrid-barrel stage before β signal exchange and β seam closure cause the release of the fully folded β barrel.

Our structural data also enable us to discriminate among a variety of previously proposed models for BAM function. We found that EspP associates with BamA to form structurally diverse hybrid-barrels during its assembly and that in two reconstructions was observed in remarkable integrated open β sheet conformations. Based on these findings we propose a β barrel folding model in which the open β sheets close toward BamA and then curl inward to form a barrel-like structure at a late stage

(Video S2). The interface between BamAβ1 and the EspP β signal does not change significantly among our 10 structures, yet the N terminus of the EspP β barrel undergoes enormous conformational changes. These observations are fundamentally inconsistent with "threading" models, which propose that unfolded OMPs enter the BamA β barrel lumen and form β hairpins that integrate sequentially into the lipid bilayer through a "lateral gate" between BamA β1 and β16 (Noinaj et al., 2017). By contrast, our structures are consistent with our previous study in which we showed that the interface between the BamA C terminus and the EspP β barrel N terminus is extremely dynamic but that the BamAβ1-β signal interface is remarkably stable during the hybrid-barrel stage *in vivo* (Doyle and Bernstein, 2019). Based on the results, we propose that the N terminus of OMP β barrels undergo a swinging action in the membrane during their assembly. In light of our structural data, we speculate that (1) at early stages of folding OMP β signals are bound by BamAβ1, (2) this interaction templates the folding of the adjacent OMP β strands via β augmentation until an elongated β sheet is formed, and (3) during the folding process the BamA β barrel transitions from an inward-open state to an outward-open state. The notion of sequential folding supports the "BamA-elongation" model (Schiffrin et al., 2017) in which the N-terminal strands of a substrate β barrel bypass the BamA β barrel altogether during β sheet elongation, except that our OS-/IO-substate structures raise the possibility that β sheet elongation and OM integration might occur simultaneously. Given recent evidence that the essential BamD subunit can bind to both the β signal and a newly identified conserved "-5-signal" (in the 5th-to-last β strand of OMPs; see Germany et al., 2021), it is also possible that the C termini of β barrels partially fold in the periplasm while associated with BamD before the β signal is transferred to BamAβ1. This idea is supported by our striking finding that helix 2 of BamD (just upstream of its "-5-signal" binding site) interacts with EspP near its "-5-signal" motif. The data suggest that our structures represent later intermediates in which the EspP "-5-signal" β strand has moved directly into the OM and away from BamD. This scenario suggests that β strands located more toward the β barrel N terminus do not require a BamA lateral gate for integration and is therefore inconsistent with sequential threading models. While this manuscript was in preparation, however, a structure of BAM bound to a fragment of EspP (containing only β9-β12) in detergent micelles was published and interpreted to support a threading model of assembly (Wu et al., 2021). In contrast to our structures, that structure showed EspP(β9-β12) bound to BamA β1 (angled toward the periplasm) and curled inward toward β16. A possible explanation for the discrepancy is the positioning of an engineered disulfide bond between EspPβ9 and BamAβ16 that would constrain the structure at a location that we have previously shown to be highly dynamic (Doyle and Bernstein, 2019). Alternatively, as EspP(β9-12) did not contain the "-5-signal," BAM may engage the fragment by an alternate mechanism relative to native assembly competent OMPs. We would also note that a few unusual OMPs including BamA and LptD, a protein that contains a lipoprotein in the lumen of its β barrel and appears to traverse the interior of the BamA β barrel during its biogenesis (Lee et al., 2019), might be assembled by alternative mechanisms.

Finally, our work yielded significant insights into the energetics of OMP assembly. First, we obtained direct experimental evidence that the C-terminal side of the BamA β barrel can modify the thickness of the membrane and may thereby lower the energy requirements for the membrane integration of OMPs. Our results are in line with MD simulations (Liu and Gumbart, 2020; Noinaj et al., 2013), *in vitro* studies that indicate that membrane thickness acts as a major barrier to OMP integration (Kleinschmidt and Tamm, 2002; Schiffrin et al., 2017), and studies that show that membrane defects accelerate β-barrel folding (Danoff and Fleming, 2015). Consistent with the membrane alterations that we observed, we also found that our native nanodiscs contained lysophospholipids, a group of lipids that has been implicated in the relaxation of frustrated bilayers and that changes in membrane curvature due to their cone-like geometry (Zheng et al., 2017). We also identified a remarkable number of polyunsaturated lipids in the nanodiscs and speculate that polyunsaturated acyl chains might be enriched in proximity to BAM in the native OM and contribute to the local membrane alterations we observed. Second, we obtained evidence that OMP assembly is not only driven by the free energy of folding but that the late stages of OMP folding are accelerated by BAM harnessing OM tension as a source of potential energy. Our experiments were inspired by an effort to explain the purpose of the deflected EspP open β sheets bound to BamA in an outward-open conformation. We proposed that the outward-open conformer of BamA holds the β signal of the folding OMP at an angle at which the intrinsic structure of the open β sheet state causes the hydrophobic transmembrane portions and aromatic girdles to deflect the OM. However, the intrinsic tension in the OM would counter this deflection and thereby force the β sheet to close into a β barrel. Consistent with our model, we demonstrated that the rate of folding after the formation of a hybrid-barrel can be transiently slowed by conditions that relax the OM and accelerated when those conditions are reversed to increase the OM tension. Furthermore, because the concentration of OMPs in the OM contributes to its rigidity, it is plausible that the mysterious "OMP-islands" (pockets in the bacterial OM with dense OMP packing and low diffusion) generate local zones of high OM stiffness that promote the high β barrel assembly activity attributed to them (Gunasinghe et al., 2018; Rassam et al., 2015; Ursell et al., 2012). From a different perspective, a rigid membrane might inhibit the integration of α-helical proteins that typically fold into fluid membranes. Given that transmembrane β barrel folding occurs in an environment that is devoid of useful energy sources, the ability of BAM to catalyze transmembrane β barrel folding by a radically different mechanism that harnesses the unusual properties of the OM might help to explain why the bacterial OM is populated almost exclusively by β barrel proteins.

Limitations of the study

Although we analyzed an extremely large number of cryo-EM images to observe multiple protein folding intermediates, we could not solve the structures of all of the possible protein folding intermediates present within our sample because the EspPβ1-BamAβ15/16 interface is extremely conformationally heterogenous. Furthermore, we cannot rule out the possibility that the BAM-^{MBP76}EspP complex exists in alternative conformations that we did not observe. Indeed, our OS and IO maps contain an unoccupied space devoid of EM density between the EspP β sheet and BamA. We have previously shown that the EspP passenger and α helix are extremely dynamic *in vivo* (Doyle and Bernstein, 2021), and it is therefore likely that, in addition to water, the cavity is at least partially filled with the traversing passenger domain and α helix, but that they were too dynamic to align during particle reconstruction. Further studies should also be performed to determine if the experimental conditions we used to decrease or increase OM tension alter the composition of the OM and whether these changes have any effect on OMP assembly. In addition, although our data show that β barrel assembly is affected by OM tension after the formation of a hybrid-barrel, we did not determine whether OM tension plays a role in earlier stages of OMP membrane integration.

STAR★METHODS

Detailed methods are provided in the online version of this paper and include the following:

- KEY RESOURCES TABLE
- RESOURCE AVAILABILITY
    - ○ Lead contact
    - ○ Materials availability
    - ○ Data and code availability
- EXPERIMENTAL MODEL AND SUBJECT DETAILS
- METHOD DETAILS
    - ○ Plasmids and plasmid construction
    - ○ Purification of BAM-$^{\text{MBP-76}}$EspP native nanodiscs
    - ○ Lipid extraction from BAM-$^{\text{MBP-76}}$EspP native nanodiscs
    - ○ LC-MS acquisition
    - ○ LC-MS data analysis
    - ○ Cryo-EM sample preparation and imaging
    - ○ Cryo-EM image processing
    - ○ Model building and refinement
    - ○ *In vivo* disulfide-bond formation assay
    - ○ Heat-modifiability/gel mobility-shift assay
    - ○ *In vivo* $^{\text{MBP-76}}$EspP assembly-restart assays
    - ○ Immunoblotting and image quantitation
- QUANTIFICATION AND STATISTICAL ANALYSIS

SUPPLEMENTAL INFORMATION

Supplemental information can be found online at https://doi.org/10.1016/j.cell.2022.02.016.

ACKNOWLEDGMENTS

This work was supported by the NIDDK and NCI Intramural Research Programs. J.R.J. is a recipient of an NIGMS MOSAIC K99/R00 award. The structural studies were performed at the NIH Multi-Institute Cryo-EM Facility (MICEF) and the NIDDK cryo-EM core facility and utilized computational resources from the NIH HPC Biowulf cluster (http://hpc.nih.gov). We thank Huaibin Wang, Haifeng He, and Bertram Canagarajah for technical support with cryo-EM and computing.

AUTHOR CONTRIBUTIONS

The study was conceived by M.T.D. and H.D.B., but all authors contributed to experimental design. The experiments, data processing, and analyses were conducted by M.T.D. and J.R.J. Lipidomic experiments and analysis were conducted by T.D., S.I.O., and M.L. The paper was written and edited by all authors. The project was supervised by J.E.H. and H.D.B.

DECLARATION OF INTERESTS

The authors declare no competing interests.

Received: August 27, 2021
Revised: December 1, 2021
Accepted: February 13, 2022
Published: March 15, 2022

REFERENCES

Adams, P.D., Afonine, P.V., Bunkóczi, G., Chen, V.B., Davis, I.W., Echols, N., Headd, J.J., Hung, L.W., Kapral, G.J., Grosse-Kunstleve, R.W., et al. (2010). Phenix: a comprehensive Python-based system for macromolecular structure solution. Acta Crystallogr. D Biol. Crystallogr. *66*, 213–221. https://doi.org/10.1107/S0907444909052925.

Anwari, K., Webb, C.T., Poggio, S., Perry, A.J., Belousoff, M., Celik, N., Ramm, G., Lovering, A., Sockett, R.E., Smit, J., et al. (2012). The evolution of new lipoprotein subunits of the bacterial outer membrane BAM complex. Mol. Microbiol. *84*, 832–844. https://doi.org/10.1111/j.1365-2958.2012.08059.x.

Barnard, T.J., Dautin, N., Lukacik, P., Bernstein, H.D., and Buchanan, S.K. (2007). Autotransporter structure reveals intra-barrel cleavage followed by conformational changes. Nat. Struct. Mol. Biol. *14*, 1214–1220. https://doi.org/10.1038/nsmb1322.

Barnard, T.J., Gumbart, J., Peterson, J.H., Noinaj, N., Easley, N.C., Dautin, N., Kuszak, A.J., Tajkhorshid, E., Bernstein, H.D., and Buchanan, S.K. (2012). Molecular basis for the activation of a catalytic asparagine residue in a self-cleaving bacterial autotransporter. J. Mol. Biol. *415*, 128–142. https://doi.org/10.1016/j.jmb.2011.10.049.

Croll, T.I. (2018). Isolde: a physically realistic environment for model building into low-resolution electron-density maps. Acta Crystallogr. D Struct. Biol. *74*, 519–530. https://doi.org/10.1107/S2059798318002425.

Danoff, E.J., and Fleming, K.G. (2015). Membrane defects accelerate outer membrane beta-barrel protein folding. Biochemistry *54*, 97–99. https://doi.org/10.1021/bi501443p.

Dautin, N., Barnard, T.J., Anderson, D.E., and Bernstein, H.D. (2007). Cleavage of a bacterial autotransporter by an evolutionarily convergent autocatalytic mechanism. EMBO J. *26*, 1942–1952. https://doi.org/10.1038/sj.emboj.7601638.

Doerner, P.A., and Sousa, M.C. (2017). Extreme dynamics in the BamA beta-barrel seam. Biochemistry *56*, 3142–3149. https://doi.org/10.1021/acs.biochem.7b00281.

Doyle, M.T., and Bernstein, H.D. (2019). Bacterial outer membrane proteins assemble via asymmetric interactions with the BamA beta-barrel. Nat. Commun. *10*, 3358. https://doi.org/10.1038/s41467-019-11230-9.

Doyle, M.T., and Bernstein, H.D. (2021). BamA forms a translocation channel for polypeptide export across the bacterial outer membrane. Mol. Cell *81*, 2000–2012.e3. https://doi.org/10.1016/j.molcel.2021.02.023.

Emsley, P., Lohkamp, B., Scott, W.G., and Cowtan, K. (2010). Features and development of coot. Acta Crystallogr. D Biol. Crystallogr. *66*, 486–501. https://doi.org/10.1107/S0907444910007493.

Fahy, E., Sud, M., Cotter, D., and Subramaniam, S. (2007). LIPID MAPS online tools for lipid research. Nucleic Acids Res. *35*, W606–W612. https://doi.org/10.1093/nar/gkm324.

Germany, E.M., Ding, Y., Imai, K., Bamert, R.S., Dunstan, R.A., Nakajima, Y., Lai, X., Webb, C.T., Stubenrauch, C.J., Hidaka, K., et al. (2021). Discovery of a conserved rule behind the assembly of β-barrel membrane proteins. Preprint at bioRxiv. https://doi.org/10.1101/2021.10.29.466387.

Gessmann, D., Chung, Y.H., Danoff, E.J., Plummer, A.M., Sandlin, C.W., Zaccai, N.R., and Fleming, K.G. (2014). Outer membrane beta-barrel protein folding is physically controlled by periplasmic lipid head groups and BamA. Proc. Natl. Acad. Sci. USA *111*, 5878–5883. https://doi.org/10.1073/pnas.1322473111.

Gorelik, A., Illes, K., and Nagar, B. (2018). Crystal structure of the mammalian lipopolysaccharide detoxifier. Proc. Natl. Acad. Sci. USA *115*, E896–E905. https://doi.org/10.1073/pnas.1719834115.

Gu, Y., Li, H., Dong, H., Zeng, Y., Zhang, Z., Paterson, N.G., Stansfeld, P.J., Wang, Z., Zhang, Y., Wang, W., and Dong, C. (2016). Structural basis of outer membrane protein insertion by the BAM complex. Nature *531*, 64–69. https://doi.org/10.1038/nature17199.

Gunasinghe, S.D., Shiota, T., Stubenrauch, C.J., Schulze, K.E., Webb, C.T., Fulcher, A.J., Dunstan, R.A., Hay, I.D., Naderer, T., Whelan, D.R., et al. (2018). The WD40 protein BamB mediates coupling of BAM complexes into assembly precincts in the bacterial outer membrane. Cell Rep. *23*, 2782–2794. https://doi.org/10.1016/j.celrep.2018.04.093.

Hagan, C.L., Wzorek, J.S., and Kahne, D. (2015). Inhibition of the beta-barrel assembly machine by a peptide that binds BamD. Proc. Natl. Acad. Sci. USA *112*, 2011–2016. https://doi.org/10.1073/pnas.1415955112.

Hart, E.M., Gupta, M., Wühr, M., and Silhavy, T.J. (2020). The gain-of-function allele bamA E470K bypasses the essential requirement for BamD in beta-barrel outer membrane protein assembly. Proc. Natl. Acad. Sci. USA *117*, 18737–18743. https://doi.org/10.1073/pnas.2007696117.

Hart, E.M., and Silhavy, T.J. (2020). Functions of the BamBCDE lipoproteins revealed by bypass mutations in BamA. J. Bacteriol. *202*, e00401–e00420. https://doi.org/10.1128/JB.00401-20.

Heinz, E., and Lithgow, T. (2014). A comprehensive analysis of the Omp85/TpsB protein superfamily structural diversity, taxonomic occurrence, and evolution. Front. Microbiol. *5*, 370. https://doi.org/10.3389/fmicb.2014.00370.

Horne, J.E., Brockwell, D.J., and Radford, S.E. (2020). Role of the lipid bilayer in outer membrane protein folding in Gram negative bacteria. J. Biol. Chem. *295*, 10340–10367. https://doi.org/10.1074/jbc.REV120.011473.

Iadanza, M.G., Higgins, A.J., Schiffrin, B., Calabrese, A.N., Brockwell, D.J., Ashcroft, A.E., Radford, S.E., and Ranson, N.A. (2016). Lateral opening in the intact beta-barrel assembly machinery captured by cryo-EM. Nat. Commun. *7*, 12865. https://doi.org/10.1038/ncomms12865.

Iadanza, M.G., Schiffrin, B., White, P., Watson, M.A., Horne, J.E., Higgins, A.J., Calabrese, A.N., Brockwell, D.J., Tuma, R., Kalli, A.C., et al. (2020). Distortion of the bilayer and dynamics of the BAM complex in lipid nanodiscs. Commun. Biol. *3*, 766. https://doi.org/10.1038/s42003-020-01419-w.

Ieva, R., and Bernstein, H.D. (2009). Interaction of an autotransporter passenger domain with BamA during its translocation across the bacterial outer membrane. Proc. Natl. Acad. Sci. USA *106*, 19120–19125. https://doi.org/10.1073/pnas.0907912106.

Ieva, R., Tian, P., Peterson, J.H., and Bernstein, H.D. (2011). Sequential and spatially restricted interactions of assembly factors with an autotransporter beta domain. Proc. Natl. Acad. Sci. USA *108*, E383–E391. https://doi.org/10.1073/pnas.1103827108.

Imai, Y., Meyer, K.J., Iinishi, A., Favre-Godal, Q., Green, R., Manuse, S., Caboni, M., Mori, M., Niles, S., Ghiglieri, M., et al. (2019). A new antibiotic selectively kills Gram-negative pathogens. Nature *576*, 459–464. https://doi.org/10.1038/s41586-019-1791-1.

Jarosławski, S., Duquesne, K., Sturgis, J.N., and Scheuring, S. (2009). High-resolution architecture of the outer membrane of the Gram-negative bacteria Roseobacter denitrificans. Mol. Microbiol. *74*, 1211–1222. https://doi.org/10.1111/j.1365-2958.2009.06926.x.

Kaur, H., Jakob, R.P., Marzinek, J.K., Green, R., Imai, Y., Bolla, J.R., Agustoni, E., Robinson, C.V., Bond, P.J., Lewis, K., et al. (2021). The antibiotic darobactin mimics a beta-strand to inhibit outer membrane insertase. Nature *593*, 125–129. https://doi.org/10.1038/s41586-021-03455-w.

Kim, S., Malinverni, J.C., Sliz, P., Silhavy, T.J., Harrison, S.C., and Kahne, D. (2007). Strcuture and function of an essential component of the outer membrane protein assembly machine. Science *317*, 961–964.

Kleinschmidt, J.H., and Tamm, L.K. (2002). Secondary and tertiary structure formation of the beta-barrel membrane protein OmpA is synchronized and depends on membrane thickness. J. Mol. Biol. *324*, 319–330. https://doi.org/10.1016/S0022-2836(02)01071-9.

Kozjak, V., Wiedemann, N., Milenkovic, D., Lohaus, C., Meyer, H.E., Guiard, B., Meisinger, C., and Pfanner, N. (2003). An essential role of Sam50 in the protein sorting and assembly machinery of the mitochondrial outer membrane. J. Biol. Chem. *278*, 48520–48523. https://doi.org/10.1074/jbc.C300442200.

Lauber, F., Deme, J.C., Lea, S.M., and Berks, B.C. (2018). Type 9 secretion system structures reveal a new protein transport mechanism. Nature *564*, 77–82. https://doi.org/10.1038/s41586-018-0693-y.

Lee, J., Sutterlin, H.A., Wzorek, J.S., Mandler, M.D., Hagan, C.L., Grabowicz, M., Tomasek, D., May, M.D., Hart, E.M., Silhavy, T.J., and Kahne, D. (2018). Substrate binding to BamD triggers a conformational change in BamA to control membrane insertion. Proc. Natl. Acad. Sci. USA *115*, 2359–2364. https://doi.org/10.1073/pnas.1711727115.

Lee, S.C., Knowles, T.J., Postis, V.L., Jamshad, M., Parslow, R.A., Lin, Y.P., Goldman, A., Sridhar, P., Overduin, M., Muench, S.P., and Dafforn, T.R. (2016). A method for detergent-free isolation of membrane proteins in their local lipid environment. Nat. Protoc. *11*, 1149–1162. https://doi.org/10.1038/nprot.2016.070.

Lee, J., Tomasek, D., Santos, T.M., May, M.D., Meuskens, I., and Kahne, D. (2019). Formation of a beta-barrel membrane protein is catalyzed by the interior surface of the assembly machine protein BamA. Elife *8*, e49787. https://doi.org/10.7554/eLife.49787.

Lessen, H.J., Fleming, P.J., Fleming, K.G., and Sodt, A.J. (2018). Building blocks of the outer membrane: calculating a general elastic energy model for beta-barrel membrane proteins. J. Chem. Theor. Comput. *14*, 4487–4497. https://doi.org/10.1021/acs.jctc.8b00377.

Leyton, D.L., Johnson, M.D., Thapa, R., Huysmans, G.H., Dunstan, R.A., Celik, N., Shen, H.H., Loo, D., Belousoff, M.J., Purcell, A.W., et al. (2014). A mortise-tenon joint in the transmembrane domain modulates autotransporter assembly into bacterial outer membranes. Nat. Commun. *5*, 4239. https://doi.org/10.1038/ncomms5239.

Lita, A., Pliss, A., Kuzmin, A., Yamasaki, T., Zhang, L., Dowdy, T., Burks, C., de Val, N., Celiku, O., Ruiz-Rodado, V., et al. (2021). IDH1 mutations induce organelle defects via dysregulated phospholipids. Nat. Commun. *12*, 614. https://doi.org/10.1038/s41467-020-20752-6.

Liu, J., and Gumbart, J.C. (2020). Membrane thinning and lateral gating are consistent features of BamA across multiple species. PLoS Comput. Biol. *16*, e1008355. https://doi.org/10.1371/journal.pcbi.1008355.

Lomize, M.A., Pogozheva, I.D., Joo, H., Mosberg, H.I., and Lomize, A.L. (2012). OPM database and PPM web server: resources for positioning of proteins in membranes. Nucleic Acids Res. *40*, D370–D376. https://doi.org/10.1093/nar/gkr703.

Lundquist, K., Bakelar, J., Noinaj, N., and Gumbart, J.C. (2018). C-terminal kink formation is required for lateral gating in BamA. Proc. Natl. Acad. Sci. USA *115*, E7942–E7949. https://doi.org/10.1073/pnas.1722530115.

Noinaj, N., Gumbart, J.C., and Buchanan, S.K. (2017). The β-barrel assembly machine in motion. Nat. Rev. Microbiol. *15*, 197–204.

Noinaj, N., Kuszak, A.J., Balusek, C., Gumbart, J.C., and Buchanan, S.K. (2014). Lateral opening and exit pore formation are required for BamA function. Structure *22*, 1055–1062. https://doi.org/10.1016/j.str.2014.05.008.

Noinaj, N., Kuszak, A.J., Gumbart, J.C., Lukacik, P., Chang, H., Easley, N.C., Lithgow, T., and Buchanan, S.K. (2013). Structural insight into the biogenesis of beta-barrel membrane proteins. Nature *501*, 385–390. https://doi.org/10.1038/nature12521.

Paramasivam, N., Habeck, M., and Linke, D. (2012). Is the C-terminal insertional signal in Gram-negative bacterial outer membrane proteins species-specific or not? BMC Genomics *13*, 510. https://doi.org/10.1186/1471-2164-13-510.

Patel, R., Hsu, S.C., Bédard, J., Inoue, K., and Jarvis, P. (2008). The Omp85-related chloroplast outer envelope protein OEP80 is essential for viability in Arabidopsis. Plant Physiol. *148*, 235–245. https://doi.org/10.1104/pp.108.122754.

Pavlova, O., Peterson, J.H., Ieva, R., and Bernstein, H.D. (2013). Mechanistic link between beta barrel assembly and the initiation of autotransporter secretion. Proc. Natl. Acad. Sci. USA *110*, E938–E947. https://doi.org/10.1073/pnas.1219076110.

Pettersen, E.F., Goddard, T.D., Huang, C.C., Couch, G.S., Greenblatt, D.M., Meng, E.C., and Ferrin, T.E. (2004). UCSF Chimera—a visualization system for exploratory research and analysis. J. Comput. Chem. *25*, 1605–1612. https://doi.org/10.1002/jcc.20084.

Pettersen, E.F., Goddard, T.D., Huang, C.C., Meng, E.C., Couch, G.S., Croll, T.I., Morris, J.H., and Ferrin, T.E. (2021). UCSF ChimeraX: structure visualization for researchers, educators, and developers. Protein Sci. *30*, 70–82. https://doi.org/10.1002/pro.3943.

Prinz, W.A., and Hinshaw, J.E. (2009). Membrane-bending proteins. Crit. Rev. Biochem. Mol. Biol. *44*, 278–291. https://doi.org/10.1080/10409230903183472.

Punjani, A., Rubinstein, J.L., Fleet, D.J., and Brubaker, M.A. (2017). cryoSPARC: algorithms for rapid unsupervised cryo-EM structure determination. Nat. Methods *14*, 290–296. https://doi.org/10.1038/nmeth.4169.

Punjani, A., Zhang, H., and Fleet, D.J. (2020). Non-uniform refinement: adaptive regularization improves single-particle cryo-EM reconstruction. Nat. Methods *17*, 1214–1221. https://doi.org/10.1038/s41592-020-00990-8.

Rassam, P., Copeland, N.A., Birkholz, O., Tóth, C., Chavent, M., Duncan, A.L., Cross, S.J., Housden, N.G., Kaminska, R., Seger, U., et al. (2015). Supramolecular assemblies underpin turnover of outer membrane proteins in bacteria. Nature *523*, 333–336. https://doi.org/10.1038/nature14461.

Rhodius, V.A., Suh, W.C., Nonaka, G., West, J., and Gross, C.A. (2005). Conserved and variable functions of the sE stress response in related genomes. PLoS Biol. *4*, e2. https://doi.org/10.1371/journal.pbio.0040002.

Rohou, A., and Grigorieff, N. (2015). CTFFIND4: fast and accurate defocus estimation from electron micrographs. J. Struct. Biol. *192*, 216–221. https://doi.org/10.1016/j.jsb.2015.08.008.

Rojas, E.R., Billings, G., Odermatt, P.D., Auer, G.K., Zhu, L., Miguel, A., Chang, F., Weibel, D.B., Theriot, J.A., and Huang, K.C. (2018). The outer membrane is an essential load-bearing element in Gram-negative bacteria. Nature *559*, 617–621. https://doi.org/10.1038/s41586-018-0344-3.

Schiffrin, B., Calabrese, A.N., Higgins, A.J., Humes, J.R., Ashcroft, A.E., Kalli, A.C., Brockwell, D.J., and Radford, S.E. (2017). Effects of periplasmic chaperones and membrane thickness on BamA-catalyzed outer-membrane protein folding. J. Mol. Biol. *429*, 3776–3792. https://doi.org/10.1016/j.jmb.2017.09.008.

Schulz, G.E. (2000). β-barrel membrane proteins. Curr. Opin. Struct. Biol. *10*, 443–447. https://doi.org/10.1016/s0959-440x(00)00120-2.

Smith, C.A., O'Maille, G., Want, E.J., Qin, C., Trauger, S.A., Brandon, T.R., Custodio, D.E., Abagyan, R., and Siuzdak, G. (2005). Metlin: a metabolite mass spectral database. Ther. Drug Monit. *27*, 747–751. https://doi.org/10.1097/01.ftd.0000179845.53213.39.

Struyvé, M., Moons, M., and Tommassen, J. (1991). Carboxy-terminal phenylalanine is essential for the correct assembly of a bacterial outer-membrane protein. J. Mol. Biol. *218*, 141–148. https://doi.org/10.1016/0022-2836(91)90880-F.

Sun, C., Benlekbir, S., Venkatakrishnan, P., Wang, Y., Hong, S., Hosler, J., Tajkhorshid, E., Rubinstein, J.L., and Gennis, R.B. (2018). Structure of the alternative complex III in a supercomplex with cytochrome oxidase. Nature *557*, 123–126. https://doi.org/10.1038/s41586-018-0061-y.

Szabady, R.L., Peterson, J.H., Skillman, K.M., and Bernstein, H.D. (2005). An unusual signal peptide facilitates late steps in the biogenesis of a bacterial autotransporter. Proc. Natl. Acad. Sci. USA *102*, 221–226. https://doi.org/10.1073/pnas.0406055102.

Tomasek, D., and Kahne, D. (2021). The assembly of beta-barrel outer membrane proteins. Curr. Opin. Microbiol. *60*, 16–23. https://doi.org/10.1016/j.mib.2021.01.009.

Tomasek, D., Rawson, S., Lee, J., Wzorek, J.S., Harrison, S.C., Li, Z., and Kahne, D. (2020). Structure of a nascent membrane protein as it folds on the BAM complex. Nature *583*, 473–478. https://doi.org/10.1038/s41586-020-2370-1.

Ursell, T.S., Trepagnier, E.H., Huang, K.C., and Theriot, J.A. (2012). Analysis of surface protein expression reveals the growth pattern of the gram-negative outer membrane. PLoS Comput. Biol. *8*, e1002680. https://doi.org/10.1371/journal.pcbi.1002680.

Voulhoux, R., Bos, M.P., Geurtsen, J., Mols, M., and Tommassen, J. (2003). Role of a highly conserved bacterial protein in outer membrane protein assembly. Science *299*, 262–265. https://doi.org/10.1126/science.1078973.

Wang, R.Y., Song, Y., Barad, B.A., Cheng, Y., Fraser, J.S., and DiMaio, F. (2016). Automated structure refinement of macromolecular assemblies from cryo-EM maps using Rosetta. Elife *5*,. https://doi.org/10.7554/eLife.17219.

Wang, X., Peterson, J.H., and Bernstein, H.D. (2021). Bacterial outer membrane proteins are targeted to the Bam complex by two parallel mechanisms. mBio *12*. e00597–21. https://doi.org/10.1128/mBio.00597-21.

Webb, C.T., Heinz, E., and Lithgow, T. (2012). Evolution of the β-barrel assembly machinery. Trends Microbiol. *20*, 612–620. https://doi.org/10.1016/j.tim.2012.08.006.

Weiss, M.S., Wacker, T., Weckesser, J., Weite, W., and Schulz, G.E. (1990). The three-dimensional structure of porin from Rhodobacter capsulatus at 3-A resolution. FEBS Lett. *267*, 268–272. https://doi.org/10.1016/0014-5793(90)80942-C.

White, P., Haysom, S.F., Iadanza, M.G., Higgins, A.J., Machin, J.M., Whitehouse, J.M., Horne, J.E., Schiffrin, B., Carpenter-Platt, C., Calabrese, A.N., et al. (2021). The role of membrane destabilisation and protein dynamics in BAM catalysed OMP folding. Nat. Commun. *12*, 4174. https://doi.org/10.1038/s41467-021-24432-x.

Wishart, D.S., Feunang, Y.D., Marcu, A., Guo, A.C., Liang, K., Vázquez-Fresno, R., Sajed, T., Johnson, D., Li, C., Karu, N., et al. (2018). HMDB 4.0: the human metabolome database for 2018. Nucleic Acids Res. *46*, D608–D617. https://doi.org/10.1093/nar/gkx1089.

Wu, R., Bakelar, J.W., Lundquist, K., Zhang, Z., Kuo, K.M., Ryoo, D., Pang, Y.T., Sun, C., White, T., Klose, T., et al. (2021). Plasticity within the barrel domain of BamA mediates a hybrid-barrel mechanism by BAM. Nat. Commun. *12*, 7131. https://doi.org/10.1038/s41467-021-27449-4.

Wu, T., Malinverni, J., Ruiz, N., Kim, S., Silhavy, T.J., and Kahne, D. (2005). Identification of a multicomponent complex required for outer membrane biogenesis in Escherichia coli. Cell *121*, 235–245. https://doi.org/10.1016/j.cell.2005.02.015.

Xiao, L., Han, L., Li, B., Zhang, M., Zhou, H., Luo, Q., Zhang, X., and Huang, Y. (2021). Structures of the β-barrel assembly machinery recognizing outer membrane protein substrates. FASEB J. *35*, e21207. https://doi.org/10.1096/fj.202001443RR.

Zheng, L., Lin, Y., Lu, S., Zhang, J., and Bogdanov, M. (2017). Biogenesis, transport and remodeling of lysophospholipids in Gram-negative bacteria. Biochim. Biophys. Acta Mol. Cell Biol. Lipids *1862*, 1404–1413. https://doi.org/10.1016/j.bbalip.2016.11.015.

Zheng, S.Q., Palovcak, E., Armache, J.P., Verba, K.A., Cheng, Y., and Agard, D.A. (2017a). MotionCor2: anisotropic correction of beam-induced motion for improved cryo-electron microscopy. Nat. Methods *14*, 331–332. https://doi.org/10.1038/nmeth.4193.

Zivanov, J., Nakane, T., Forsberg, B.O., Kimanius, D., Hagen, W.J., Lindahl, E., and Scheres, S.H. (2018). New tools for automated high-resolution cryo-EM structure determination in RELION-3. Elife *7*, e42166. https://doi.org/10.7554/eLife.42166.

STAR★METHODS

KEY RESOURCES TABLE

REAGENT or RESOURCE	SOURCE	IDENTIFIER
Antibodies		
Monoclonal mouse anti-StrepII	Qiagen	cat#34850
Monoclonal mouse anti-His	Genescript	cat#A00186
Monoclonal mouse anti-LPS	HycultBiotech	cat#HM6011
Polyclonal rabbit anti-BamD	Pavlova et al., 2013	N/A
Polyclonal rabbit anti-EspP β-barrel (C-term peptide)	Szabady et al., 2005	N/A
Goat anti-mouse Ig 800CW IRDye	Licor	cat#926-32210
Goat anti-rabbit Ig 680LT IRDye	Licor	cat#926-680210
Bacterial and virus strains		
E. coli B strain BL21(DE3)	Invitrogen	cat#C600003
E. coli K-12 strain XL1-Blue	Agilent	cat#200236
E. coli K-12 strain NEB5alpha	NEB	cat#C2987H
Chemicals, peptides, and recombinant proteins		
4,4’-dipyridyl disulfide	Sigmaaldrich	cat#143057-5G
Proteinase K	Roche	cat#3115852001
Xiran SL30010P20	Orbiscope	cat#SMALP200
Deposited data		
BAM-MBP-76EspP high-resolution structure	This paper	EMDB-26114, PDB: 7TTC
BAM-MBP-76EspP class 1 structure	This paper	EMDB-26105, PDB: 7TSZ
BAM-MBP-76EspP class 2 structure	This paper	EMDB-26106, PDB: 7TT0
BAM-MBP-76EspP class 3 structure	This paper	EMDB-26108, PDB: 7TT2
BAM-MBP-76EspP class 4 structure	This paper	EMDB-26107, PDB: 7TT1
BAM-MBP-76EspP class 5 structure	This paper	EMDB-26109, PDB: 7TT3
BAM-MBP-76EspP class 6 structure	This paper	EMDB-26110, PDB: 7TT4
BAM-MBP-76EspP open-sheet EspP state structure	This paper	EMDB-26111, PDB: 7TT5
BAM-MBP-76EspP intermediate-open EspP state structure	This paper	EMDB-26112, PDB: 7TT6
BAM-MBP-76EspP barrelized EspP/continuous open BamA state structure	This paper	EMDB-26113, PDB: 7TT7
Oligonucleotides		
See Table S2 in Supplemental information	This paper	N/A
Recombinant DNA		
See Table S2 in Supplemental information	This paper	N/A
Software and algorithms		
UCSF Chimera	Pettersen et al., 2004	https://www.cgl.ucsf.edu/chimera/
UCSF ChimeraX	Pettersen et al., 2021	https://www.cgl.ucsf.edu/chimerax/
RELION 3.1	Zivanov et al., 2018	https://relion.readthedocs.io/en/latest/Installation.html
cryoSPARC	Punjani et al., 2020	https://cryosparc.com
Coot	Emsley et al., 2010	https://www2.mrc-lmb.cam.ac.uk/personal/pemsley/coot/
Isolde	Croll, 2018	https://isolde.cimr.cam.ac.uk

(*Continued on next page*)

Continued

REAGENT or RESOURCE	SOURCE	IDENTIFIER
Rosetta	Wang et al., 2016	https://www.rosettacommons.org/software
Phenix	Adams et al., 2010	https://phenix-online.org
Other		
OPM server	Lomize et al., 2012	https://opm.phar.umich.edu/ppm_server

RESOURCE AVAILABILITY

Lead contact

Further information and requests for resources and reagents should be directed to and will be fulfilled by the lead contact, Harris D. Bernstein (harris_bernstein@nih.gov).

Materials availability

Strains and plasmids generated in this study are available upon request to the lead contact.

Data and code availability

- Structural data supporting findings in this study have been deposited in the Protein Data Bank (PDB) and the Electron Microscopy Data Bank (EMDB). The accession codes of the cryo-EM maps and accompanying atomic models have been provided for: (1) BAM-$^{MBP-76}$EspP *high-resolution* (EMDB-26114, PDB: 7TTC): (2) BAM-$^{MBP-76}$EspP *class 1* (EMDB-26105, PDB: 7TSZ): (3) BAM-$^{MBP-76}$EspP *class 2* (EMDB-26106, PDB: 7TT0): (4) BAM-$^{MBP-76}$EspP *class 3* (EMDB-26108, PDB: 7TT2): (5) BAM-$^{MBP-76}$EspP *class 4* (EMDB-26107, PDB: 7TT1): (6) BAM-$^{MBP-76}$EspP *class 5* (EMDB-26109, PDB: 7TT3): (7) BAM-$^{MBP-76}$EspP *class 6* (EMDB-26110, PDB: 7TT4): (8) BAM-$^{MBP-76}$EspP *open-sheet EspP state* (EMDB-26111, PDB: 7TT5): (9) BAM-$^{MBP-76}$EspP *intermediate-open EspP state* (EMDB-26112, PDB: 7TT6): (10) BAM-$^{MBP-76}$EspP *barrelized EspP/ continuous open BamA state* (EMDB-26113, PDB: 7TT7).
- This paper does not report original code.
- Any additional information required to reanalyze the data reported in this paper is available from the lead contact upon request.

EXPERIMENTAL MODEL AND SUBJECT DETAILS

The *E. coli* B strain BL21(DE3) (Invitrogen catalog number C600003) was used for all experiments and *E. coli* K-12 strains XL1-Blue (Agilent catalog number 200236) or NEB5α (NEB catalog number C2987H) were routinely used for cloning and mutagenesis. Strains were grown in Lysogeny Broth (LB) (Miller or Lenox formulation as indicated) supplemented with ampicillin (100 μg mL^{-1}) and/or trimethoprim (50 μg mL^{-1}) as necessary.

METHOD DETAILS

Plasmids and plasmid construction

Oligonucleotides and plasmids used in this study are listed in Table S2. When necessary, BAM (^{His}BamABCDE) was expressed from an IPTG inducible promoter in plasmid pMTD372 and $^{MBP-76}$EspP was expressed from a *P*rhaB inducible promoter in plasmid pMTD607 (Doyle and Bernstein, 2019). Plasmids expressing cysteine substitution mutant derivatives of pMTD372 and pMTD607 were generated using the Q5 Site-Directed Mutagenesis Kit (NEB catalog number E0554S).

Purification of BAM-$^{MBP-76}$EspP native nanodiscs

E. coli strain BL21(DE3) transformed with plasmids expressing ^{His}BamA$_{S425C}$BCDE and $^{MBP-76}$EspP$_{S1299C}$ were grown overnight in LB (Miller) at 25 °C. Overnight cultures were then washed and resuspended in fresh LB (1 culture volume) before inoculating 16 Thomson Ultra Yield flasks (each containing 1 L of LB (Miller)) at a starting OD$_{600}$ of 0.05. Cultures were grown for 4 h (25 °C, 250 rpm), induced with 0.4 mM IPTG for 1 h, and then induced for a further 45 min with 0.2% L-rhamnose. Each culture was pelleted (5,000 x *g*, 10 min, 4 °C), resuspended in 50 mL ice-cold phosphate buffered saline (PBS; 9 g L^{-1} NaCl, 0.144 g L^{-1} KH$_2$PO$_4$, 0.795 g L^{-1} Na$_2$HPO$_4$, pH 7.4), and transferred to an Erlenmeyer flask on ice. Bacteria in each flask were treated with a final concentration of 0.4 mM 4-DPS (4,4′-dipyridyl disulfide; a thiol-specific disulfide oxidizing catalyst) for 30 min with orbital shaking at 100 rpm in packed ice, pelleted (4,500 x *g*, 10 min, 4 °C), resuspended in 25 mL ice-cold PBS containing SigmaFast EDTA free protease inhibitors (PI), and then frozen in liquid nitrogen. All 400 mL of harvested bacteria were thawed and then lysed with a Constant Systems Cell

Disruptor (15,000 psi, cooled to 5 °C). Cell debris was removed (20,000 x *g*, 15 min, 4 °C) and then the lysate was ultracentrifuged (194,903 x *g*, 2 h, 4 °C) to harvest membrane pellets. Using a Dounce homogenizer, membranes were homogenized in 55 mL native-nanodisc buffer (3 % Xiran SL30010P20 (Orbiscope), 50 mM TrisHCl, 500 mM NaCl, 10 % glycerol, 1 mM EDTA, pH 8) containing freshly added PI and incubated at 4 °C for 5 h with constant inversion. The solution was ultracentrifuged (265,455 x *g*, 40 min, 4 °C) and then the supernatant was collected and diluted 1:2 with a buffer (50 mM TrisHCl, 500 mM NaCl, 10 % glycerol, pH 8 at 4 °C) containing freshly added PI. The diluted protein solution was then incubated with 25 mL StrepTactin XT superflow resin (IBA GmbH) at 4 °C overnight with constant inversion. The protein-resin solution was then transferred to a gravity column (all column steps mentioned hereafter were conducted at 4 °C) and the protein flow-through was passed over the resin a second time. The resin was washed with 10 x 50 mL TN buffer (50 mM TrisHCl, 500 mM NaCl, pH 8) at 4 °C before BAM-$^{\text{MBP-76}}$EspP native nanodiscs were eluted with 150 mL biotin buffer (50 mM biotin, 50 mM TrisHCl, 500 mM NaCl, pH 8) at 4 °C. To concentrate and further purify the sample, imidazole (20 mM final) was added to the eluted protein which was subsequently incubated with 5 mL NiNTA resin (Qiagen) at 4 °C overnight with constant inversion. The protein solution was then transferred to a gravity column and the protein flow-through was passed over the resin twice more. The resin was washed with 3 x 10 mL of a buffer (20 mM imidazole, 50 mM TrisHCl, 500 mM NaCl pH 8) at 4 °C before BAM-$^{\text{MBP-76}}$EspP native nanodiscs were eluted with 15 mL of elution buffer (500 mM imidazole, 50 mM TrisHCl, 150 mM NaCl pH 8) at 4 °C. The eluted protein was desalted and exchanged into TN$^{\text{low}}$ buffer (50 mM TrisHCl, 150 mM NaCl, pH 8 at 4 °C) using Sephadex G-25 PD-10 desalting columns (Cytiva) following the manufacturers protocol before concentrating to a volume of 20-50 μL using an Amicon Ultra 0.5 mL concentrator (10 kDa cut-off). BAM-$^{\text{MBP-76}}$EspP native nanodiscs were used immediately in grid-preparations. For each preparation, correct folding was confirmed by heat-modifiability/mobility-shift assays.

Lipid extraction from BAM-$^{\text{MBP-76}}$EspP native nanodiscs

To extract lipids from of BAM-$^{\text{MBP-76}}$EspP native nanodiscs (20 μL), Bligh-Dyer biphasic extraction was conducted essentially as described previously (Lita et al., 2021). An equivalent volume of desalting buffer was used as a control. Briefly, 880 μL of water was added to each sample and the samples were snap-frozen on dry ice. Samples were thawed, sonicated for 30 sec at 30 % amplitude, and vortexed for 10 sec (medium speed). 520 μL of methanol (MeOH) was added and the samples were vortexed for 10 sec and incubated for 10 min on ice. 500 μL of chilled chloroform was then added and the samples were vortexed for 15 sec before being incubated for 30 min on ice. Samples were then centrifuged (12,000 x g, 20 min, 4 °C) to separate aqueous (upper) and hydrophobic (lower) phases. Finally, the hydrophobic phase was transferred to a 1.5 mL tube and evaporated at room temperature under a dry nitrogen stream (Lita et al., 2021).

LC-MS acquisition

All mobile phase and reagents were composed of LC-MS grade additives and Optima™ LC-MS Grade solvents (Fisher Scientific, USA) unless otherwise indicated. LC-MS data was acquired via an Agilent 6545 QTOF with a dual Agilent Jet Stream (AJS) electrospray ionization (ESI) source coupled with an Infinity II 1290 UHPLC system using conditions as previously described (Lita et al., 2021). Extracted lipids were mixed with 100 μL of 80:20 MeOH/water. Lipidomic features were resolved using an Acquity UPLC CSH 1.7 μm, 2.1 × 50 mm C18 column (Waters Corp. MA, USA) with a mobile phase gradient consisting of acetonitrile (ACN)/water (30:70) containing 5 mM ammonium formate and 0.15 %(v/v) formic acid (Solvent A) and isopropanol (IPA)/ACN (90/10) containing 10 mM ammonium formate and 0.15 %(v/v) formic acid (Solvent B) at a column temperature of 45 °C and flow rate of 0.250 mL min^{-1}. In ESI negative (-) mode, hydrophobic extracts were resolved using gradient: 0–0.1 min, 1 % B; 0.8 min, 5 % B, 2.0 min, 35 % B; 4.5 min 38 % B; 4.75 min, 40 % B; 7.5 min, 71 % B; 8.5 min, 80.5 % B; 9.5 min, 91.5 % B; 11 min, 98 % B; 12.25 min, 100 %; 12.5 min, 99 % B; 13.5 min, 1 % B re-equilibration for 1.5 min. The following MS parameters were applied: injection volume, 7.5 μL; drying gas temperature (temp), 150 °C; gas flow, 7 L min^{-1}; nebulizer, 45 psi; sheath gas temp, 350 °C; sheath gas flow, 12 L min^{-1}; capillary voltage, 3000 V; nozzle voltage, 25 V; fragmentor, 90 V; skimmer, 50 V; scan rate, 3.0 spectra sec^{-1}. In ESI positive (+) mode, hydrophobic extracts were resolved using: 0–0.1 min, 1 % B; 0.3 min, 5 % B, 1.75 min, 35 % B; 4.25 min 38 % B; 4.5 min, 40 % B; 7.25 min, 71 % B; 9.25 min, 98 % B; 10.25 min, 100 % B; 10.5 min, 99 % B; 11.25 min, 1 % B re-equilibration for 1.5 min. MS parameters were applied as follows: injection volume, 7 μL; drying gas temp, 150 °C; gas flow 6 L min^{-1}; nebulizer, 40 psi; sheath gas temp, 350 °C; sheath gas flow, 12 L min^{-1}; capillary voltage, 3500 V; nozzle voltage, 35 V; fragmentor, 150 V; skimmer, 50 V; scan rate, 3.0 spectra sec^{-1}. Wash cycles consisting of strong wash (50 % MeOH, 25 % IPA, and 25 % water), seal wash (10 % IPA and 90 % water) and needle wash (50 % IPA) were used to eliminate carryover between consecutive injections (Lita et al., 2021).

LC-MS data analysis

During acquisition, the buffer extract was injected in both negative and positive ESI modes prior to the BAM-$^{\text{MBP-76}}$EspP native nanodisc extract to correct for background ions. Agilent Masshunter Qualitative Analysis B.10.0 was utilized to detect and assign putative identifications to ions based on accurate mass within ± 5 mDa to matches in an in-house Agilent Personal Compound Database and Library (PCDL) that was composed of lipid classes of interest (PG, PE and CL). All putative hits detected from ESI± modes were incorporated into target lists (.csv). To verify the putative IDs, the m/z target lists were uploaded to a targeted MS/MS method and tandem MS analysis was conducted using collision energies of 10V and 40V, MS scan rate of 3 spectra sec^{-1}, and MS/MS scan rate of 1 spectra sec^{-1} with narrow detection window of 1.3 m/z (which is the lowest MS/MS fragment detection range available for the QTOF instrument). Parent ions and their corresponding fragment spectra were extracted using Agilent Masshunter Qualitative Analysis B.8.0 and compared to LC-MS/MS reference spectra available via Metlin, Lipid Maps, and Human Metabolome Database (HMDB) online libraries (Smith et al., 2005; Fahy et al., 2007; Wishart et al., 2018).

Cryo-EM sample preparation and imaging

BAM-$^{MBP-76}$EspP native nanodiscs were diluted in TN^{low} buffer at a concentration of ∼2 – 8 mg L^{-1}, and 3 μL of sample was applied onto glow-discharged C-flat grids (EMS CF-1.2/1.3-4Au-50) for 3 sec before plunge freezing in liquid ethane using a Leica EM Grid Plunger (Leica Microsystems). Datasets were collected at the NIH Multi-Institute Cryo-EM Facility (MICEF) using a Titan Krios G3 microscope (Thermo-Fisher) operating at 300 kV. During 4 collection sessions (Figure S2, dataset 1) micrographs were collected at a magnification of 130,000x (calibrated pixel size 0.5371 Å, nominal defocus range 0.6 to 1.8 μm, 40 frames, and 60 $e^-/Å^2$ electron exposure per movie) using a Gatan K2 Summit direct electron detection camera equipped with a Gatan Quantum LS imaging energy filter with slit width set to 20 eV. After the microscope was upgraded with a Gatan K3 camera an additional collection session (Figure S2; dataset 2) was conducted at a magnification of 105,000x (calibrated pixel size 0.4281 Å, nominal defocus range 0.6 to 1.8 μm, 23 frames, and 60 $e^-/Å^2$ electron exposure per movie). Multiple collection sessions were conducted in order to allow reconstructions of multiple intermediate substates of the complex that were present in the sample.

Cryo-EM image processing

Movie frames of BAM-$^{MBP-76}$EspP cryo-electron micrographs were motion corrected and dose-weighted with MotionCor2 in RELION 3.1 (Zheng et al., 2017a; Zivanov et al., 2018). CTF estimation was determined in RELION 3.1 using Ctffind4 (Rohou and Grigorieff, 2015). Initial particle picking was done with the Laplacian-of-Gaussian-based autopicking. Picked particles were processed to generate an initial 3D reference for autopicking in RELION 3.1. A total of 25,393,510, particles, from dataset 1 collected on the K2 camera, and 9,873,900 particles, from dataset 2 on the K3 camera, were picked. Following one round of 2D classification and three rounds of 3D classification 3,996,756 particles from both datasets were merged with pixel size of 1.07 Å /pixel. Because we aimed to visualize intermediate folding states of EspP, we performed focused classification 3D classification on the 3,996,756 million particles after signal subtraction of heterogenous BamA P3, BamB, and BamD N-terminus components, which yielded a subset of 1,187,709 particles. These particles produced a 4.4 Å map using RELION 3.1. Following CTF refinement and particle polishing, the 1,187,709 particles were processed by three strategies in parallel using RELION 3.1 (Figure S2). Strategy 1 generated a 4.2 Å map after 3D refinement. Strategy 2 used 3D classification of the 1,187,709 particles in RELION 3.1 to reveal six classes of the BAM-$^{MBP-76}$EspP complex. Strategy 3 used focused classification and refinement after signal subtraction of BamA P3, BamB, and BamD N-terminus revealed three folding states of EspP. Particles from strategy 1, the six classes in strategy 2, and the 3 states in strategy 3 were moved from the RELION 3.1 pipeline to cryoSPARC for further cryo-EM image processing (Punjani et al., 2017, 2020). Following pruning of the particle sets by rounds of heterogenous refinement and final refinements, the following cryo-EM maps were obtained: (1) a 3.6 Å map of BAM-$^{MBP-76}$EspP from strategy 1; (2) six cryo-EM maps capturing the motion in the soluble subunits of BAM-$^{MBP-76}$EspP from strategy 2 [class 1 (4.5 Å), class 2 (4.3 Å), class 3 (4.2 Å), class 4 (4.3 Å), class 5 (4.3 Å), and class 6 (4.2 Å)]; (3) three cryo-EM maps following focused classification/refinement of the substrate region produced the OS-state (4.3 Å), IO-state (4.3 Å), and the B/CO-state (4.8 Å) stemming from strategy 3. Local resolution filtered maps were produced in cryoSPARC.

Model building and refinement

Initial fitting of BAM-$^{MBP-76}$EspP subunits into cryo-EM maps was done manually in UCSF Chimera (Pettersen et al., 2004) using Bam complex subunits from PDB 5D0O (Gu et al., 2016), EspP from PDB 2QOM and 3SLJ (Barnard et al., 2007, 2012), and lipopolysaccharide from PDB: 5W7B (Gorelik et al., 2018). For the high-resolution 3.6 Å map, manual building/corrections of BamA subunits, EspP and LPS was done in Coot 0.9 and Isolde followed by model refinement using Rosetta and real-space refinement in Phenix (Adams et al., 2010; Croll, 2018; Emsley et al., 2010; Wang et al., 2016). The high-resolution atomic model derived from the 3.6 Å map was used as a starting model for building models of the six classes (from strategy 2) and the three focused states (from strategy 3). Because the substrate region in the focused maps is observed at low resolution, some of the EspP β-barrel N-terminus was docked into the map. The membrane interacting regions of EspP were better defined, could be identified by the orientations of proteins in OPM server (Lomize et al., 2012), and modeled into the cryo-EM map using Rosetta, Coot and Isolde (Croll, 2018; Emsley et al., 2010; Wang et al., 2016). The cryo-EM data collection, final refinement, and validation statistics for the 10 atomic models are presented in Table S3. Structural analysis, measurements and figures were prepared in Chimera and ChimeraX (Pettersen et al., 2021).

In vivo disulfide-bond formation assay

To observe site-specific interactions between BamD and the EspP β-barrel *in vivo*, disulfide-bond formation assays were conducted essentially as described (Doyle and Bernstein, 2019, 2021). Briefly, strains containing appropriate plasmids were grown overnight from a single colony in 10 mL LB (Miller) at 25 °C with orbital shaking (250 rpm). Cultures were pelleted (3000 x g, 5 min, 4 °C), washed with 10 mL LB (Miller), and resuspended in 10 mL LB (Miller) before inoculating 10 mL LB (Miller) subcultures at OD_{600} = 0.05. After cultures were grown for 4 h (25 °C, 250 rpm) to OD_{600} ∼0.4 - 0.6, a final concentration of 0.4 mM IPTG was added to induce expression of BAM for 1 h. Subsequently, a final concentration of 0.2% L-rhamnose was added to induce expression of $^{MBP-76}$EspP for 45 min. 1 mL samples were aliquoted into tubes on ice, pelleted (10,000 x g, 2 min, 4 °C), resuspended in 1 mL of ice-cold PBS, and incubated on ice with 4-DPS at a concentration of 0.2 mM (or an equivalent volume of ethanol for mock treatment controls). After 30 min, samples were pelleted (10,000 x g, 2 min, 4 °C) and resuspended in 0.5 mL ice-cold PBS. Bacteria were then lysed and proteins were precipitated by adding a final concentration of 10% (v/v) trichloroacetic acid (TCA) and 4 mM phenylmethanesulfonyl fluoride (PMSF) to the cell suspension and incubating for 10 min on ice. The precipitated proteins were pelleted (20,817 x g, 10 min, 4 °C), washed with 0.6 mL ice-cold acetone, re-pelleted, and air-dried at 37 °C for 20 min. Proteins were resuspended in 2x SDS protein gel loading solution (Quality Biological) in a volume normalized to an OD_{600} measurement recorded immediately as subculture samples were taken (volume in μL = 200 x OD_{600}). Samples were heated to 99 °C for 15 min and aliquots (5 μL) resolved by SDS-PAGE on 8 % – 16 % Tris-glycine minigels (Invitrogen) (150 V, 1 h 47 min, room temperature) before being transferred to nitrocellulose for immunoblot analysis.

Heat-modifiability/gel mobility-shift assay

To observe the folded states of the BamA-EspP hybrid-barrel, purified BAM-$^{MBP-76}$EspP native nanodiscs were diluted 1:9 in ice-cold TN buffer before aliquots were further diluted 1:9 in modified loading buffer (2x SDS protein gel loading solution serially diluted 1:1 with 20 % glycerol twice and then 1:1 again with TN buffer for a final SDS concentration of 0.5%) on ice. Aliquots were either heated to 99 °C for 10 min or retained on ice and proteins were immediately resolved by cold-SDS-PAGE (gel tank in packed ice, running at 150 V, 4 °C cold room). Gels were subsequently Coomassie Brilliant Blue (R-250) stained to detect proteins.

In vivo $^{MBP-76}$EspP assembly-restart assays

To monitor the final stages of assembly of EspP after the formation of a hybrid-barrel intermediate with BamA, bacteria containing plasmids that express BAM and $^{MBP-76}$EspP were cultured overnight from a single colony in 10 mL LB (Lenox) at 25 °C with orbital shaking (250 rpm). Cultures were pelleted (4,000 x g, 3 min, 4 °C), washed with LB (Lenox), and resuspended in 10 mL LB (Lenox) before inoculating 10 mL LB (Lenox) subcultures at OD_{600} = 0.05. To create a pool of molecules at a hybrid-barrel intermediate stage of assembly in bacteria, subcultures were grown and the expression of BAM and $^{MBP-76}$EspP was induced as in the disulfide-bond formation assays described above. Aliquots (1 mL samples) were then pelleted (10,000 x g, 2 min, 20 °C), resuspended in equivalent volumes of either LB (Lenox) or LB (Lenox) containing 0.8 M sorbitol (LB-Sorbitol), and pre-incubated in a Thermomixer (Eppendorf) (20 °C, 350 rpm). After 5 min pre-incubation, 200 μg mL^{-1} PK (or an equivalent volume of 50 mM TrisHCl pH 8 for mock-treated controls) was added and bacteria were incubated (20 °C, 350 rpm) for 0, 2, 5, 10, and 20 min. For experiments requiring media exchange from LB-Sorbitol, samples incubated with PK for 5 min were pelleted (15,000 x g, 20 s, 20 °C), resuspended in 1 mL of either LB (Lenox) or LB-Sorbitol (media pre-equilibrated to 20 °C), and further incubated (20 °C, 350 rpm) until 10 or 20 min after PK addition. For experiments requiring disulfide-crosslinking, bacteria incubated with PK for 5 min were pelleted (15,000 x g, 20 s, 4 °C), resuspended on ice in 1 mL ice-cold LB (Lenox) or LB-Sorbitol (matching the previous incubation medium for each sample), and incubated on ice for 2 min in the presence of 4-DPS (0.2 mM final concentration). To stop reactions at required time-points, bacteria were pelleted (15,000 x g, 20 s, 4 °C), resuspended in 0.5 mL ice-cold LB (Lenox) or LB-Sorbitol (matching the previous incubation medium for each sample), and TCA precipitated as described above. Precipitated proteins were solubilized and resolved by SDS-PAGE as described above. For a set of control experiments, induced bacterial cultures (1 mL aliquots) were incubated with LB or LB-Sorbitol for 5 min as above and pelleted (15,000 x g, 20 s, 4 °C). The culture media supernatant was retained, filtered (0.22 μm pore), and both cell pellet and supernatant were TCA precipitated.

Immunoblotting and image quantitation

The iBlotII transfer device (Life Technologies) was routinely used to transfer protein gels to nitrocellulose membranes. Immunoblotting buffer [Odyssey Blocking Buffer (Li-Cor) and PBS (mixed together at a 1:1 ratio)] supplemented with 0.01 % Tween-20 was used for blocking steps and as a diluent for primary and secondary antibodies. Monoclonal mouse anti-StrepII, anti-His, and anti-LPS antibodies were obtained from QIAGEN (catalog number 34850), Genscript (catalog number A00186), and HycultBiotech (catalog number HM6011), respectively. Polyclonal rabbit anti-BamD and anti-$EspP_{\beta C}$ have been described previously (Pavlova et al., 2013; Szabady et al., 2005). Infra-red Goat anti-mouse Ig secondary antibodies (anti-mouse 800CW IRDye, catalog number 926-32210) or anti-rabbit Ig (anti-rabbit 680LT IRDye, catalog number 926-680210) were obtained from Li-Cor. Membranes were blocked overnight and incubated with primary antibodies for 18 h at room temperature, washed twice with PBS-T (PBS supplemented with 0.01 % Tween-20), incubated for 2 h with secondary antibodies, and washed twice with PBS-T and three times with PBS before air drying (37 °C, 20 min). Dried membranes were scanned using maximum quality and resolution settings with an Amersham Typhoon 5 imager (GE Healthcare) outfitted with 785 nm and 685 nm lasers and IRlong 825BP30 and IRShort 720BP20 filters. Within-lane pixel intensities were measured using Fiji software (v2.0.0-rc-68/1.52 g) and used to calculate the fraction of the band of interest relative to other bands of interest [e.g. for assembly restart assays, the fraction of folded EspP β-barrel was determined by using the formula [folded EspP β-barrel/sum of EspP signals)].

QUANTIFICATION AND STATISTICAL ANALYSIS

All statistical analyses were conducted using GraphPad Prism (v9.1.0). Details of the number of experiments (N), definition of center, and variance measurements are noted in the figure legends. Significant differences were defined as a P value <0.05.

Supplemental figures

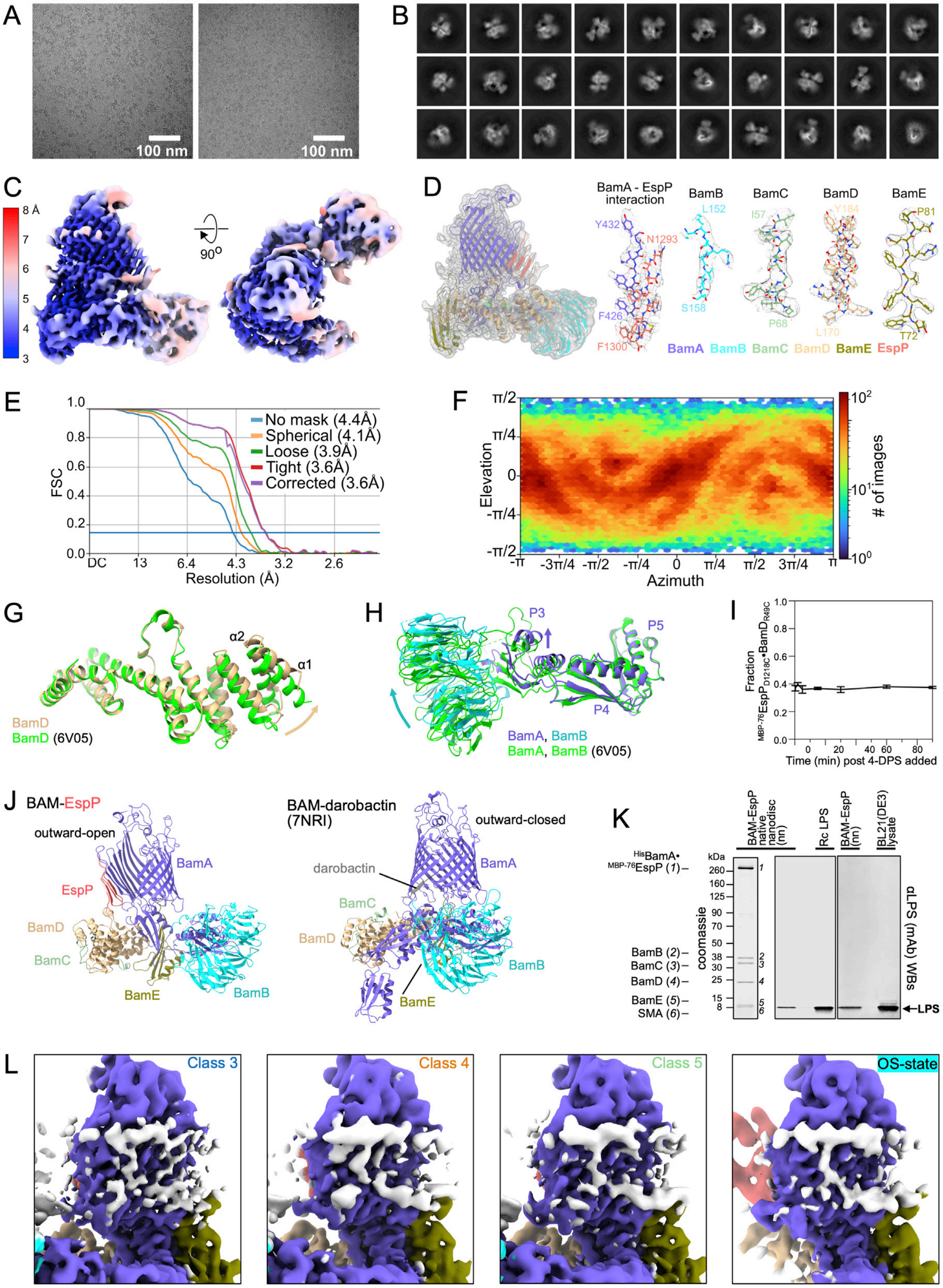

(legend on next page)

Figure S1. Generation and validation of BAM-$^{\text{MBP-76}}$EspP high-resolution map, atomic model and lipid/LPS stabilization, in relation to Figures 1 and 2

(A) Representative cryo-EM micrographs of BAM-$^{\text{MBP-76}}$EspP OM nanodiscs.

(B) Representative 2D classes.

(C) Map colored by local resolution.

(D) Left, BAM-$^{\text{MBP-76}}$EspP atomic model in the map (colors as in Figure 1). Right, representative fits of BamA-EspP β barrel hybridization interface and BamB-E models to the map.

(E) Gold-standard Fourier shell correlation (FSC).

(F) Orientation distribution of particles used in reconstruction.

(G) BAM-BamA$_{\Delta L1}$ hybrid-barrel (PDB: 6V05) (green) aligned with the BAM-$^{\text{MBP-76}}$EspP model (on BamA POTRA5 residues Y348-R421). Only BamD is shown (colors as in Figure 1). Compared with BAM-BamA$_{\Delta L1}$, the N-terminal α helices of the BamD subunit in the BAM-$^{\text{MBP-76}}$EspP structure expand toward the membrane.

(H) As in (G) except showing only BamA POTRA domains P3-5 and BamB. For BAM-$^{\text{MBP-76}}$EspP, P3 and BamB are shifted toward the membrane.

(I) *E. coli* BL21(DE3) expressed $^{\text{His}}$BamABCD$_{\text{R49C}}$E and $^{\text{MBP-76}}$EspP$_{\text{D1218C}}$ as in Figure 1E, except that samples were taken at multiple time points after the addition of the 4-DPS oxidant (±SEM, n = 3).

(J) Side-by-side comparison of the BAM-$^{\text{MBP-76}}$EspP structure and the structure of BAM inhibited by darobactin (PDB: 7NRI) to show the conformational changes in the BamA β barrel (inward-open versus inward-closed) and the rotation of accessory lipoproteins/POTRA domains.

(K) Components of BAM-$^{\text{MBP-76}}$EspP native nanodiscs were separated by SDS-PAGE and Coomassie stained (left) or subjected to immunoblot (WB) with a monoclonal antibody (mAb) that recognizes *E. coli* lipopolysaccharide (LPS). A total cell extract from strain BL21(DE3) and purified LPS derived from an Rc LPS producing strain of *E. coli* (which is essentially the same size as BL21(DE3) LPS) (Sigma L5014) were used to provide molecular weight markers. For the total cell extract, *E. coli* BL21(DE3) was grown to OD$_{600}$ = 1 in LB at 37°C. A cell pellet from 1 mL of culture was resuspended in 100 μL of 2× SDS protein gel loading solution and boiled for 15 min prior to SDS-PAGE.

(L) Lipid/LPS stabilization during OMP assembly is apparent in multiple different maps. Views of selected maps with proteins colored as in Figure 1 and high-density stabilized membrane components colored in white. Density consistent with lipid A head groups and a stabilized acyl chain in the high-resolution map in Figure 2 is also reproduced in independently derived maps.

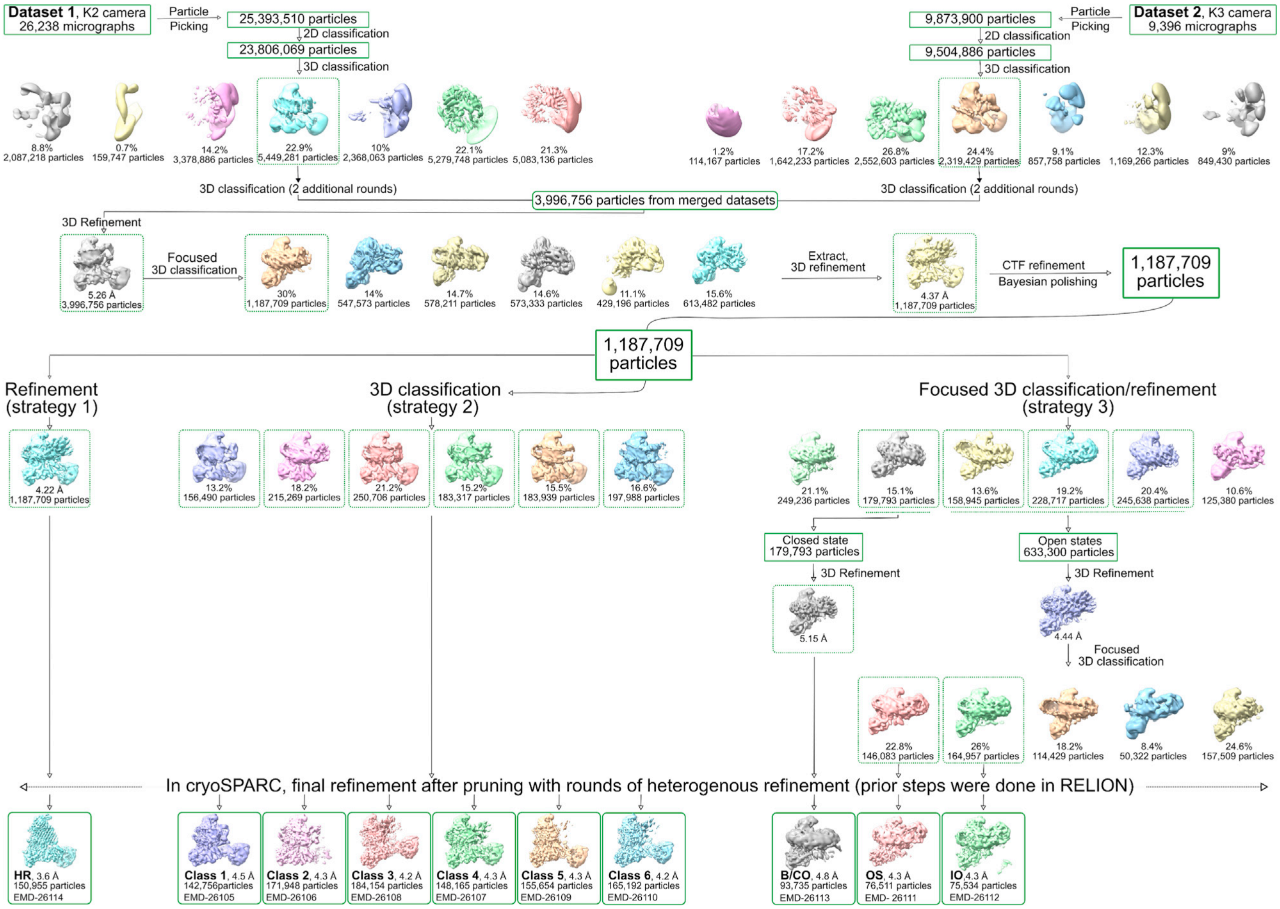

Figure S2. Flowchart of BAM-$^{MBP-76}$EspP cryo-EM reconstructions, related to STAR Methods

The flowchart outlines the processing approaches that led to the high-resolution (HR) map, the six whole-particle classes (Classes 1–6), and the open-sheet (OS), intermediate-open (IO), and barrelized/continuous-open (B/CO) focused reconstructions.

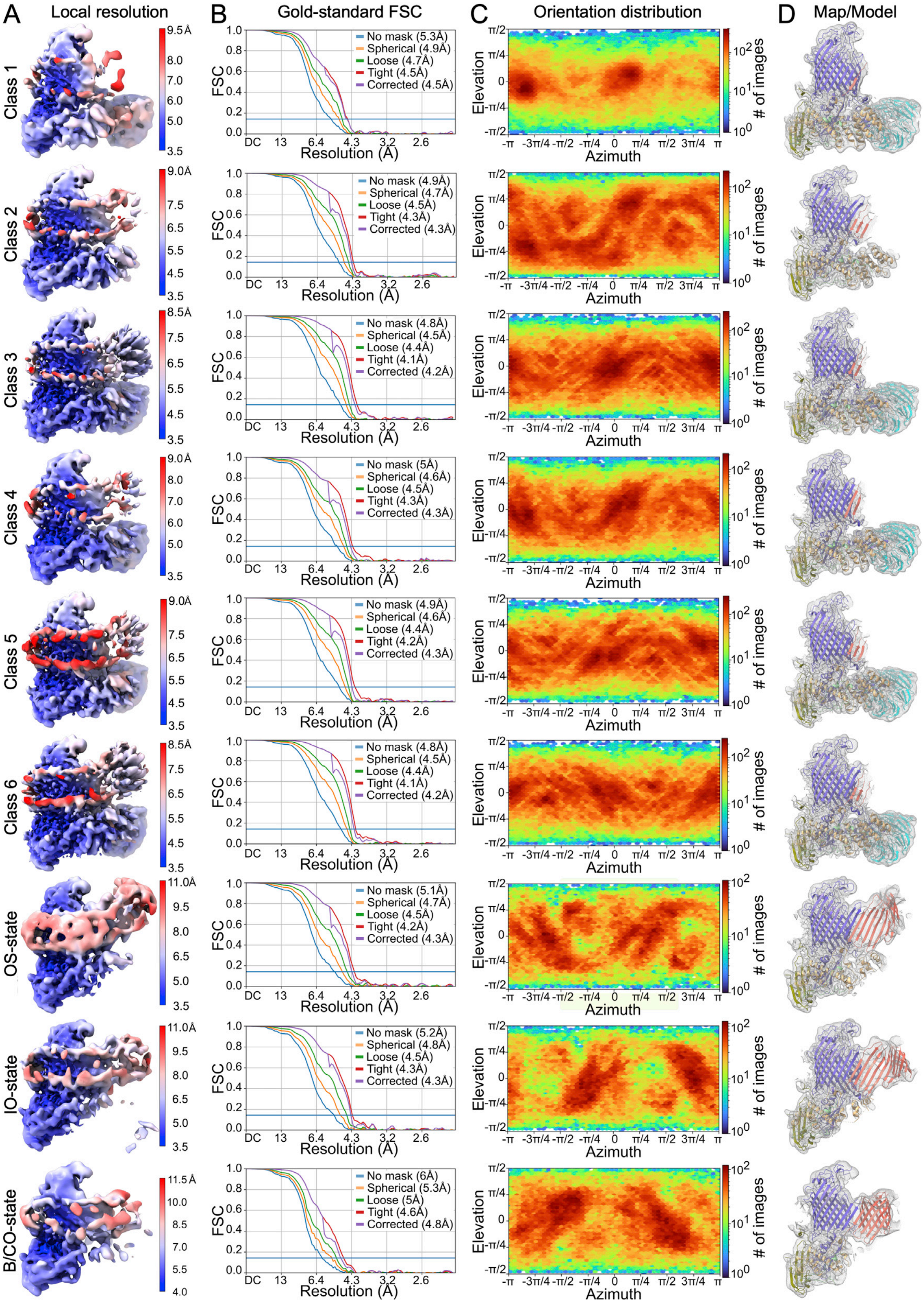

(legend on next page)

Figure S3. Validation of BAM-$^{\text{MBP-76}}$EspP whole-particle maps (Classes 1–6) and focused maps, related to Figures 3 and 4

(A) Column shows each reconstructed cryo-EM map colored by local resolution.

(B) Column shows gold-standard Fourier shell correlation (FSC) curves for each map.

(C) Column shows orientation distributions of particles used in each reconstruction.

(D) Column shows refined BAM-$^{\text{MBP-76}}$EspP atomic models within each map.

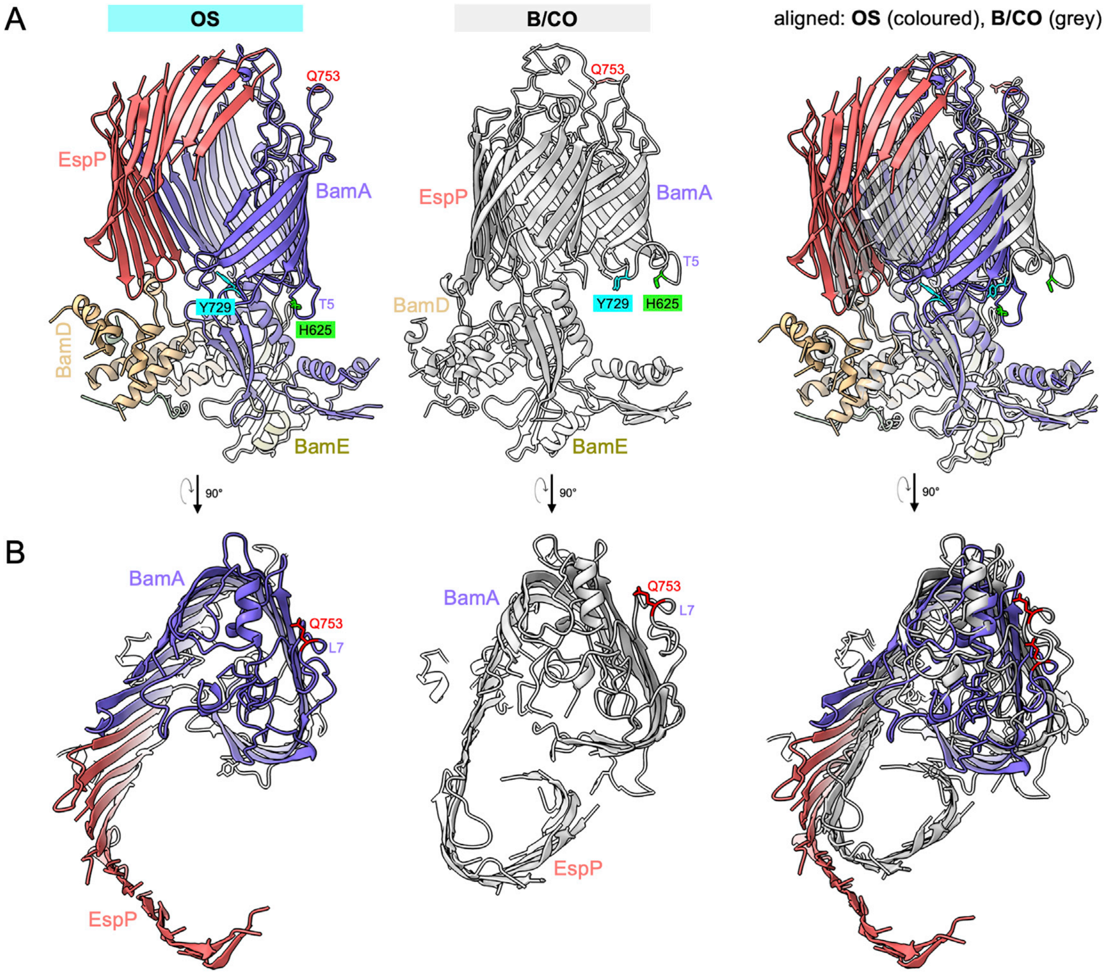

Figure S4. Comparison of open-sheet (OS) and barrelized/continuous-open (B/CO) BamA-EspP asymmetric hybrid-barrel states, related to Figure 4

(A and B) Comparisons of OS and B/CO states as in Figure 4D, except that side (A) and extracellular (B) views of the entire models are shown. Colors and labeling as in Figure 4. The EspP β sheet and the BamA β barrel exhibit major conformational changes between the OS and B/CO states, whereas the conformations of the periplasmic components of BAM remain essentially identical between the two states.

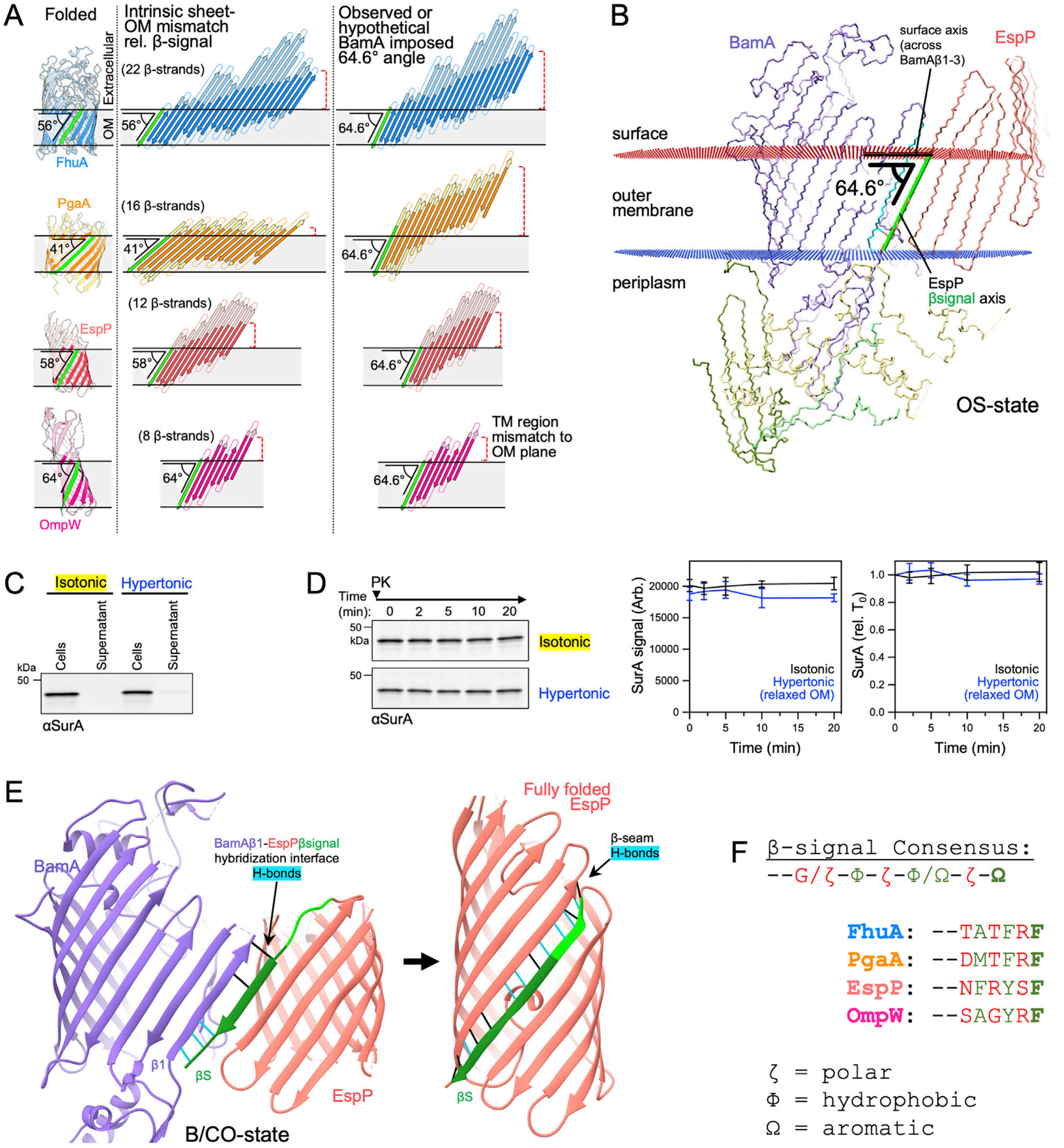

Figure S5. BamA accentuated angular antagonism of incompletely folded β barrels, assembly-restart assay controls, and instability of the hybrid-barrel state, related to Figure 5

(A) *E. coli* β barrels of varied sizes (FhuA; PDB 1FCP, PgaA; PDB 4Y25, EspP; 2QOM, OmpW; PDB 2F1V) (left column) were hypothetically unraveled (middle column) with the position of the conserved β signal (green) held constant to its orientation when fully folded, showing intrinsic mismatch between the membrane plane and the transmembrane portion of β strands (dark shade of each strand). Right column shows expanded β sheets at a hypothetical BamA-imposed angle (extrapolated from measured angle of EspP β signal when bound to BamA). We speculate that BamA holds OMPs at a high angle to harness OM tensile forces to accelerate β barrel folding.

(B) The BAM-$^{MBP-76}$EspP OS-state model shown with membrane plane based on the BAM subunits (OPM server; Lomize et al., 2012). The β signal axis (green) was calculated with the membrane spanning backbone. The surface axis (black) was calculated across BamA β strands 1–3. The angle between the surface and β signal axes is 64.6°.

(legend continued on next page)

(C) *E. coli* BL21(DE3) expressing $^{\text{His}}$BamABCDE and $^{\text{MBP-76}}$EspP were suspended in LB (isotonic control) or LB-sorbitol (hypertonic) for 5 min as in Figure 5C. Proteins from the bacterial pellet and culture supernatant were isolated and analyzed by immunoblotting with an antiserum against periplasmic chaperone SurA (αSurA) (n = 4).
(D) The levels of SurA in the samples from Figure 5C were monitored by immunoblotting with αSurA. Left, representative blots. Right, quantified raw SurA signal or SurA signal relative to the 0-min time point (T_0).
(E) The hybridization interface of the BAM-$^{\text{MBP-76}}$EspP B/CO-state has fewer hydrogen (H) bonds than the β seam of fully folded EspP (PDB: 2QOM). H-bonds were identified using Chimera FindHBond that fit the precise criteria (cyan) or with relaxed tolerances (0.4 Å/20.0°) (black). Dark green = 1,292–1,300.
(F) The consensus sequence for the Gram-negative OMP β signal motif (as described by Kaur et al., 2021) and an alignment of the six C-terminal residues of the OMPs in (A) to the consensus sequence are shown.